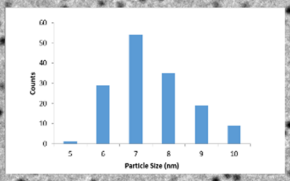


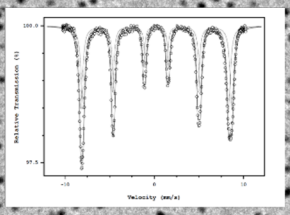


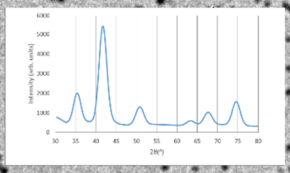


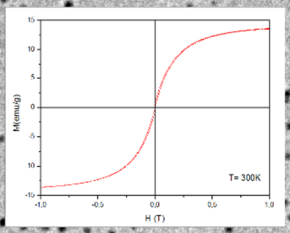


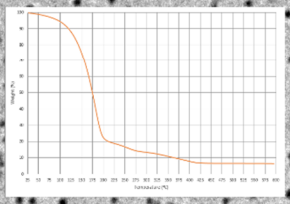

Nuno André da Silva Gaspar

# DEVELOPMENT OF A BIODEGRADABLE NANOPROBE

Dissertation presented to the University of Coimbra to complete the necessary requirements for obtaining the degree of Master of Science in Biomedical Engineering, held under scientific orientation of Maria Benilde Faria de Oliveira e Costa, PhD and Luísa Maria Rocha Durães, PhD

September 2014

· U C ·

UNIVERSIDADE DE COIMBRA

· U C ·

FCTUC FACULDADE DE CIÊNCIAS
E TECNOLOGIA
UNIVERSIDADE DE COIMBRA

Nuno André da Silva Gaspar

# Desenvolvimento de uma Nanosonda Biodegradável

*Dissertação apresentada à Universidade de Coimbra para cumprimento dos requisitos necessários à obtenção do grau de Mestre em Engenharia Biomédica*

Orientadores:
Maria Benilde Faria de Oliveira e Costa (CEMDRX, Dep. de Física)
Luísa Maria Rocha Durães (CIEPQPF, Dep. de Engenharia Química)

Coimbra, 2014

Este trabalho foi desenvolvido em colaboração com:

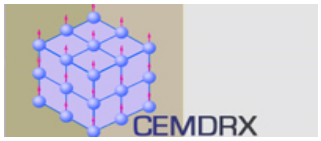


*Choose a job you love and you will never have to work a day in your life*

(Confucius)

# Acknowledgements

I would like to thank my supervisors, Dr. Benilde Costa and Dr. Luisa Durães, for having the honour and privilege of working with them, for all the guidance provided and the necessary support throughout the course of this work. I would also like to thank Dr. Nuno Rocha for advising during the early stages of this work.

I would like also to acknowledge Professor Friedrich Wagner from the Technical University of Munich for making possible Mössbauer spectroscopy at 4.2 K. Dr. Judes Gonçalves dos Santos, from the Federal University of Rondônia in Brazil, without his collaboration the Amazonian essential oils incorporation wouldn't exist as part of this work. Dr. Vladimir Khomchenko (CEMDRX) help proved to be invaluable in the early analysis of XRD data. I'd also want to thank Professor José António Paixão, coordinator of CEMDRX, who made possible for the XRD analysis to be performed to our samples. I'd also want to acknowledge Professor Vitor Amaral from the University of Aveiro for the knowledge provided and for making VSM analysis possible. I'd also want to thank Dr. Sofia Lima from REQUIMTE (Faculty of Pharmacy of University of Porto) for the help provided in the cytotoxicity exams performed to our samples.

I would like to also thank all the people from the research group for an excellent working environment, providing assistance whenever it was necessary. I'd like to leave a special thank you note for Engineer Telma Matias for the help provided throughout the course of the experimental work.

To my family, without their support and comprehension the making of this thesis wouldn't be possible.

To all my friends, whom were always there in pivotal points of my life whether they were good or bad moments.

# Abstract

Currently, the demand for higher quality magnetic nanoparticles for use as a magnetic nanoprobe to assist in medical imaging techniques and cancer therapy by hyperthermia has been high. Moreover, recent results regarding the phytochemistry benefits that some Amazonian essential oils possess have sparkled great interest in developing methods to use these oils in various medical treatments.

The main objective of this work is to develop a biodegradable magnetic nanoprobe which allies the superparamagnetism versatility of iron oxide nanoparticles with the benefits associated with *Copaiba* and *Andiroba*'s oils.

In order to improve the capabilities of this biodegradable magnetic nanoprobe, the synthesis method that originates the superparamagnetic iron oxide nanoparticles (SPIONs) was studied and certain paths were tested in order to improve that reaction product. Also, the cytotoxicity of the SPIONs was studied as well as the ability and effects of incorporating the SPIONs in Amazonian essential oils.

Particle size obtained for SPIONs was around 6 nm. Mössbauer and XRD analysis indicate maghemite as their main iron oxide phase. Also, small traces of magnetite proved to be present in some samples. VSM results showed a magnetization saturation of 57 emu/g, at 7 K, and 42 emu/g, at 300 K. After incorporating the SPIONs in *Copaiba* and *Andiroba* essential oils these values dropped which indicates that a blocking effect occurs when the Amazonian oils are incorporated with SPIONS.

All the obtained results from the characterization data performed on the various samples seem promising towards having a biodegradable magnetic nanoprobe of SPIONs incorporated in Amazonian essential oils. Although, some unexpected results that were obtained will require further study and development.

**Keywords:** SPIONs; Amazonian essential oils; *Copaiba*; *Andiroba*; biodegradable magnetic nanoprobe; Mössbauer spectroscopy; XRD; VSM.

# Resumo

Actualmente, há uma grande procura por nanopartículas magnéticas de alta qualidade para uso como nanosonda magnética em técnicas de imagiologia médica e no tratamaneto de cancro por hipertermia. Por outro lado, óleos oriundos da floresta Amazónica têm despertado cada vez maior interesse em possíveis tratamentos médicos devido às suas qualidade fitoterapêuticas.

O objectivo principal deste trabalho será desenvolver uma nanosonda magnética biodegradável que alie a versatilidade associada ao superparamagnetismo das nanopartículas de óxidos de ferro com os benefícios associados aos óleos de *Copaiba* e de *Andiroba*.

De modo a melhorar as capacidades desta nanosonda biomagnética, o método de síntese que origina estas nanopartículas superparamagnéticas de óxidos de ferro (SPIONs) foi estudado e certos caminhos foram testados de forma a melhorar o produto da reacção. Também, a citotoxicidade das SPIONs foi estudada, assim como a viablilidade e os efeitos da incorporação das SPIONs nos óleos essenciais da Amazónia.

O tamanho de partícula obtido para as SPIONs é cerca de 6 nm. Análises recorrendo a espectroscopia de Mössbauer e XRD revelam que a maghemite é o principal óxido de ferro presente nas nossas amostras. Contudo, pequenas quantidades de magnetite podem ser encontradas em certas amostras. Os resultados obtidos por VSM deram uma saturação de magnetização de 42 emu/g, a 300 K, e de 57 emu/g, a 7 K. Após incorporação do óleo de Copaíba e do óleo de Andiroba estes valores baixaram significativamente, indicando a presença de um efeito de bloqueio devido aos óleos Amazónicos.

Todos os resultados obtidos da caracterização feita às várias amostras parecem promissores na obtenção de uma nanosonda magnética biodegradável que incorpore óleos essenciais da Amazónia com as SPIONs. No entanto, alguns resultados inesperados que foram obtidos ao longo do decurso deste trabalho irão requerer um trabalho futuro mais aprofundado.

# Table of Contents

# List of Figures

# List of Tables

# Acronyms

SPIONs – Superparamagnetic Iron Oxide Nanoparticles

MRI – Magnetic Resonance Imaging

$Fe_3O_4$ – Magnetite

$\gamma$-$Fe_2O_3$ – Maghemite

XRD – X-Ray Diffraction

FWHM – Full Width at Half Maximum

VSM – Vibrating Sample Magnetometer

FTIR – Fourier Transform Infra-Red

TGA – Thermal Gravimetric Analysis

DSC – Differential Scanning Calorimetry

TEM – Transmission Electron Microscopy

IS – Isometric Shifting

QS – Quadrupole Splitting

DLS – Dynamic Light Scattering

# 1. Introduction

The ability to control and direct nanoparticles through the bloodstream to a specific target by using an external magnetic field has always been of great interest to biomedical applications. Standing at the forefront of this technology are the superparamagnetic iron oxide nanoparticles (SPIONs).

Their inherent superparamagnetism renders them the ability of behaving like a giant paramagnetic atom granting a fast response to applied magnetic fields with negligible reminiscence and coercivity. This characteristic makes them ideal for biomedical applications since it diminishes the risk of forming agglomerates [1].

SPIONs must be biocompatible and non-toxic, but other characteristics can also be added to make them have a broader use. Because of their oxidative instability, SPIONs must have a protective shell against degradation. This shell can also be used to bind specific drugs, proteins, enzymes, antibodies and other molecular targets [2].

Conventional imaging techniques, like magnetic resonance imaging (MRI), lack the combination of high sensitivity and high spatial resolution. Thus the use of SPIONs can greatly increase sensitivity needed to perform high resolution molecular imaging [2]. The use of SPIONs in cancer treatments by hyperthermia have also been in development and show promising results [3].

Research has gathered great interest towards Amazonian essential oils over the last years. The search for a scientific explanation to the benefits of these oils shown in folk medicine has reached promising results. *Copaiba* [4] and *Andiroba* [5] are among those oils who have been proving their benefits.

Therefore, the development of a biodegradable magnetic nanoprobe using SPIONs and Amazonian essential oils seemed to be an obvious way. During the course of this work we will assess not only the reaction synthesis of these nanoparticles, but also the development done towards improving it. For last, we

will observe, compare and take notes of changes in the SPIONs when they are incorporated into *Copaiba* and *Andiroba* essential oils.

## 1.1. Objectives and motivation

We propose ourselves in this work to study into further detail the synthesis of the iron oxide nanoparticles obtained by thermal decomposition of iron acetylacetonates. Several modifications to the initial procedure will be made to have a better understanding of the process. We will be focusing on several aspects that might affect the reaction, such as: the use of different iron precursors ratios, nucleation time and surfactant substitution. Besides devoting our time to study the effect of some synthesis parameters on the iron oxide nanoparticles characteristics, we'll also spend some of it observing the effects that Amazonian oils might have on the properties of the produced nanoparticles.

Mössbauer spectroscopy and XRD will be the main techniques used to determine the formed iron oxide phases. TEM will serve as a method to accurately determine the nanoparticles' size. FTIR will be used to confirm the presence of the chemical groups of the protective shell surrounding the nanoparticles. VSM will allows us to know the magnetic effect the nanoparticles suffer when incorporated in *Copaiba* and *Andiroba*'s oils. The samples will also be subjected to cytotoxic exams to confirm their biocompatibility.

As motivation, it is expected that this work will contribute to a better understanding of the studied nanoparticles synthesis method and their properties, as well as the effects/changes when they are incorporated in Amazonian essential oils. We hope this will help to further develop the application of a biodegradable magnetic nanoprobe incorporating SPIONs in Amazonian essential oils.

## 1.2. Thesis outline

This thesis is comprised of five chapters and is organized as follows.

Chapter 1 presents both the objectives and the motivation of this work. A brief summary of contents present in the following chapters will also be made.

Chapter 2 consists of basic concepts related to magnetism and the type of magnetization phenomenon that nanoparticles produced in this work manifest. Furthermore, the basic principles needed to understand the characterization techniques used in this work will be explained.

Chapter 3 will focus on enlightening the experimental methodology used. Every step taken from the original synthesis methods based on literature to the methods developed and the experimental assembly used throughout the course of this work will be explained in this chapter. This chapter will also be devoted to how samples were prepared to be used in the different characterization techniques.

Chapter 4 will present and discuss the obtained results. Once we reach the end of this chapter, all the routes that were taken will hopefully be explained and refuted by solid data.

Chapter 5 will mark the end of this work. In this chapter, conclusions will be presented and suggestions for future works will be formulated.

# 2. Basic Concepts

## 2.1. Magnetism

Magnetism has been studied since ancient Greece was thriving with knowledge. Lodestone, a naturally magnetized form of the mineral magnetite, was one of the first subjects related to magnetism studied by Greek scholars and philosophers. From this study the most basic application of magnetism was invented, the magnetic compass [6].

In condensed matter systems there are interesting effects that we can found. First, atoms should possess magnetic moments. Second, these moments should interact somehow [6].

There is a surprisingly rich variety of magnetic properties that can be found in real systems. This is explained by the diversity of types of magnetic interactions dependent on whether or not magnetic moments can act together in a cooperative way [6].

### 2.1.1. Diamagnetism, paramagnetism and ferromagnetism

There's always a duality in materials due to their magnetic susceptibility. This means that an applied magnetic field will induce a magnetic moment which either opposes or aligns itself with the direction of the magnetic field which caused it. According to its behaviour we call it diamagnetic or paramagnetic material, correspondingly [6].

However, it's not that simple. That's because all materials exhibit some degree of diamagnetism. Thus, there is always a balance of diamagnetic versus paramagnetic effect. Depending on what effect overcomes the other we have a diamagnetic or a paramagnetic material [6].

In paramagnetic materials the magnetic moments point in random directions when there's no longer an applied magnetic field to the material. This random orientation is explained by the weak interactions with neighbouring atoms. The magnetization of a paramagnetic material will depend on the ratio of the applied magnetic field versus the temperature of the material. In practice, an increase in

the applied magnetic field will line up the spins but an increase in the temperature of the material will randomize the spins [6].

There's also another main type of magnetism called ferromagnetism. In this case, when the material is subjected to an applied magnetic field, it aligns itself with it and keeps its magnetic moment even after the applied magnetic field ceases. Contrary to the paramagnetic and diamagnetic effects, the ferromagnetic one is very strong [6].

One way to differentiate diamagnetic, paramagnetic and ferromagnetic materials is by measuring their bulk magnetic susceptibility ($\chi$). If $\approx -10^{-5}$ , it's diamagnetic. If $\chi \approx 10^{-3} - 10^{-5}$, it's paramagnetic. And finally, if $\chi \approx 50 - 10^{4}$ it's ferromagnetic [7].

### 2.1.2. Ferrimagnetism

Ferrimagnetism is a specific type of ferromagnetic interactions which one can find on ferrites. This magnetic phenomenon is explained by how the two sublattices that make up the crystallographic arrangement interact with each other. When the magnetization of the sublattices is not equal and opposite then they can't cancel each other out, resulting in a net magnetization of the material. Also, the sublattices will have quite different temperature dependence because the molecular field on each sublattice is different. This means that one sublattice can dominate the magnetization at lower temperature but the other dominates at higher temperature. When this happens, the net magnetization will be reduced to zero and changes sign at a temperature known as the compensation temperature [6].

### 2.1.3. Superparamagnetism

Low dimensionality can lead to subtle, complex and ultimately useful changes in magnetic behaviour of the system.

Reducing the particle size has its own consequences on how the system will behave below a certain critical size. The particles no longer behave as a multi-domain system and become a single-domain one. That's explained in terms of energy. They assume a single-domain formation when the cost of domain wall formation doesn't outweigh any saving in demagnetizing energy, resulting in a

single-domain particle constrained to lie parallel or anti-parallel to the direction of an applied magnetic field [6].

If we consider a distribution of particles in a non-magnetic matrix and assume that each particle is sufficiently far apart so that no interparticle interaction takes place, then this system will behave like a paramagnetic one except that each independent moment is no longer atomic but a large group of moments. Each of those groups is inside each and every particle of our system. And this is what we can call a superparamagnetic system [6].

When having small particle sizes the magnetization direction fluctuates instead of being stable.

It is assumed that the magnetic anisotropy in nanoparticles is uniaxial with the magnetic anisotropy energy given by the simple expression:

$$E(\theta) = kV \sin^2 \theta \quad (1)$$

Where *k* is the magnetic anisotropy constant, *V* is the particle volume and *θ* is the angle between the magnetization direction and the easy direction of magnetization.

According to the equation, there are energy minima at *θ*=0º and *θ*=180º separated by an energy barrier *kV*. If this energy barrier is comparable to or smaller than the thermal energy, the magnetization direction of a magnetic nanoparticle may fluctuate spontaneously between the easy directions corresponding to the two minima. This phenomenon is known as superparamagnetic relaxation.

For non-interacting particles the relaxation time, i.e., the average time between two magnetization reversals is for $^{kV}/_{k_0 t} \geq 1$ given by the Néel-Brown expression:

$$\tau = \tau_0 \exp(^{kV}/_{k_0 t}) \quad (2)$$

$\tau_0$ is typically in the range of $10^{-13}$-$10^{-9}$ s.

## 2.2. Iron oxides

Iron oxides are common compounds found in nature. Due to their wide spread in nature, many different scientific disciplines studied and shared knowledge

about them. Whether it's a biomineral in Biology to a catalyst in Industrial Chemistry, iron oxides have been widely used throughout [8].

There are sixteen known iron oxides and, from these, six of them are made of only iron and oxygen. Our object of study will only be two of those six: magnetite and maghemite. In table 1, a brief summary of some physicochemical properties that can allows us to distinguish between these such similar and interchangeable iron oxides is presented [8].

**Table 1 - Physicochemical properties of Magnetite (Fe3O4) and Maghemite (γ-Fe2O3) [8].**

| **Mineral** | **Magnetite ($Fe_3O_4$)** | **Maghemite ($\gamma$-$Fe_2O_3$)** |
|---|---|---|
| **Colour** | Black | Reddish-brown |
| **Density ($g.cm^{-3}$)** | 5.18 | 4.87 |
| **Crystallographic structure** | Cubic | Cubic or tetragonal |
| **Cell dimensions (nm)** | 0.8396 | 0.8347 |
| **Type of magnetism at Room Temperature** | Ferrimagnetic | Ferrimagnetic |
| **Curie Temperature (K)** | 850 | 820-986 |
| **Magnetization saturation at 300 K (emu/g)** | 92-100 | 60-80 |

## 2.2.1. Magnetite

Magnetite ($Fe_3O_4$) is a black ferrimagnetic iron oxide, with a Curie transition temperature ($T_C$) of 850 K and a Verwey transition temperature ($T_V$) of 120 K. Having an inverse spinel structure containing both $Fe^{2+}$ and $Fe^{3+}$ as shown by figure 1. Below the Verwey transition temperature, the species of $Fe^{2+}$ and $Fe^{3+}$ arrange themselves in a regular pattern giving rise to a normal spinel structure [8].

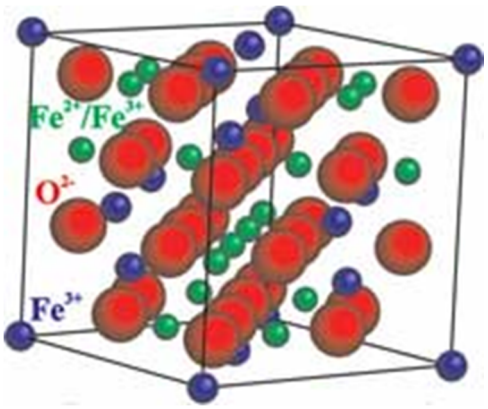


**Figure 1 – Crystallographic structure of magnetite (inverse spinel).**

It was one of the first iron oxides being studied by XRD in order to determine the details of its crystallographic structure. It is defined by having a face-centred cubic unit cell on an inverse spinel structure with a unit cell edge length of 0.8396 nm. Since magnetite contains both divalent ($Fe^{2+}$) and trivalent ($Fe^{3+}$) iron atoms, they occupy their two main crystal sites in different ways. Tetrahedral sites (A sites) are occupied by $Fe^{3+}$. Octahedral sites (B sites) are distributed between $Fe^{2+}$ and $Fe^{3+}$. Due to their close packing structure, $Fe^{2+}$ and $Fe^{3+}$ ions change places with each other. This phenomenon accounts for the good electrical conductivity exhibited by this iron oxide. Frequently, magnetite can be slightly metal deficient on $Fe^{3+}$ octahedral sites. As a result of those vacancies, its stoichiometric $Fe^{2+}/Fe^{3+}$ ratio of 0.5 is often not achieved [8].

The two different cation sites in the structure (A and B sites) form two interpenetrating magnetic sublattices with antiparallel spins. Although equal in spin direction, their magnetic magnitudes are not. This ultimately results in ferrimagnetism at room temperature. When magnetite particles have a size below 6 nm, the magnetic system assumes a superparamagnetic behaviour [8].

The mixed valence of iron in magnetite makes it thermodynamically unstable at atmospheric $O_2$ pressure [9]. Because of this, magnetite is much more susceptible to oxidation. A research was made where magnetite synthetic crystals were oxidized. The intermediates obtained from this had decreasing levels of $Fe^{2+}$ in its composition. Although crystal size and morphology remained unaltered, its cell edge did not. The unit cell edge ranged from 0,8338 to 0,8389 nm (see, for comparison, table 1) [8].

### 2.2.2. Maghemite

Maghemite ($\gamma$-$Fe_2O_3$) is a reddish-brown ferrimagnetic iron oxide with the same inverse spinel structure as magnetite. The main difference between their structures is the cation deficient octahedral sites of maghemite resulting in a cubic unit cell value of 0,83474 nm, which is slightly below the unit cell value for magnetite [8].

In fact, maghemite only has trivalent state iron, thus the divalent iron atoms that occupy the octahedral sites in magnetite are vacant in maghemite. This makes the magnetic structure of maghemite composed by one sublattice in the

tetrahedral and another in the octahedral sites. The spin sublattices orientations are both antiparallel with a difference of magnitude between each other, resulting in ferrimagnetic behaviour at room temperature. When maghemite particles have a size below 10 nm, the magnetic system behaves superparamagnetically at room temperature [8].

## 2.3. Synthesis of magnetic nanoparticles

There are several methods described in the literature for synthesis of magnetic nanoparticles in solution, from co-precipitation to thermal decomposition, microemulsion or even hydrothermal synthesis. All of them are known to produce high-quality, highly stable, shape-controlled and monodispersed nanoparticles. These methods have been not only used to produce magnetite and maghemite, they were also used to synthesise other ferrites like $MgFe_2O_4$ and $CoFe_2O_4$. Table 2 presents a summary comparing all the different synthesis methods [1].

**Table 2 - Comparison between different synthesis methods of magnetic nanoparticles [1].**

| Method | Synthesis | Reaction temp. (ºC) | Reaction period | Solvent | Size distribution | Shape control | Yield |
|---|---|---|---|---|---|---|---|
| **Thermal decomposition** | Complex, inert atmosphere | 100-320 | Hours - days | Organic | Very narrow | Very good | High, scalable |
| **Hydrothermal synthesis** | Simple, high pressure | 220 | Hours-days | Water-ethanol | Very narrow | Very good | Medium |
| **Co-precipitation** | Very simple, ambient conditions | 20-90 | Minutes | Water | Relatively narrow | Poor | High, scalable |
| **Microemulsion** | Complex, inert atmosphere | 20-50 | hours | Organic | Relatively narrow | Good | Low |

As shown in table 2, thermal decomposition shows a very narrow size distribution of particles produced as well as containing a high and scalable yield. This fits perfectly on the requisites that are required for our work.

### 2.3.1. Thermal decomposition

Thermal decomposition will be the nanoparticle synthetic route used throughout this work. As a result of this, we will now focus on the description of the mechanisms involved in this type of nanoparticles' synthesis.

This method is based on the thermal decomposition of organometallic compounds in high-temperature boiling organic solvents containing stabilizing surfactants. The most often used organometallic precursors are acetylacetonates, being fatty acids, oleic acid or oleylamine the more commonly used surfactants [1].

One of the important aspects of this synthesis is the ratio between reagents. It is decisive for the control of the size and morphology of the obtained nanoparticles. Reaction temperature and time play also an important role in this aspect of the process, as well as the posterior aging period [1].

Nanoparticles formed by thermal decomposition follow a sol formation mechanism known as nucleation process where a control of the initial number or particles followed by their subsequent growth is essential. However, in order to better understand this process we must consider nucleation and crystal growth processes in more detail [10].

Thermodynamically, there's a balance between the energy released by the formation of the new solid phase and the energy needed to form the surface of small nuclei of this new phase. Thus, the surface free energies govern the growth of colloidal particles. Molecules will then be exchanged among the particles so that they can achieve equilibrium with the solution surrounding them. An important aspect to be considered is the critical size, above which clusters will tend to grow. In a dispersion that contains particles with multiple sizes, a diffusional flow of solutes moves from the smaller particles to the larger ones [10].

The model used to explain nucleation and growth from a supersaturated system is described by La Mer. When the reaction is started, the dissolved solute increases at a steady rate. When the concentration reaches a critical supersaturation point, nucleation starts to occur. At a certain moment, nucleation starts to cause a decrease in concentration. In this point of the reaction, particle growth will replace particle nucleation. Concentration will continue to decrease, due to growth mediated by diffusion, until it reaches an equilibrium solubility value [10].

An interesting aspect of this process is that the more nuclei formed at the beginning of the process, the smaller will be the particles obtained. This is explained because a given amount of mass is going to be distributed to a greater number of nucleation centres [10].

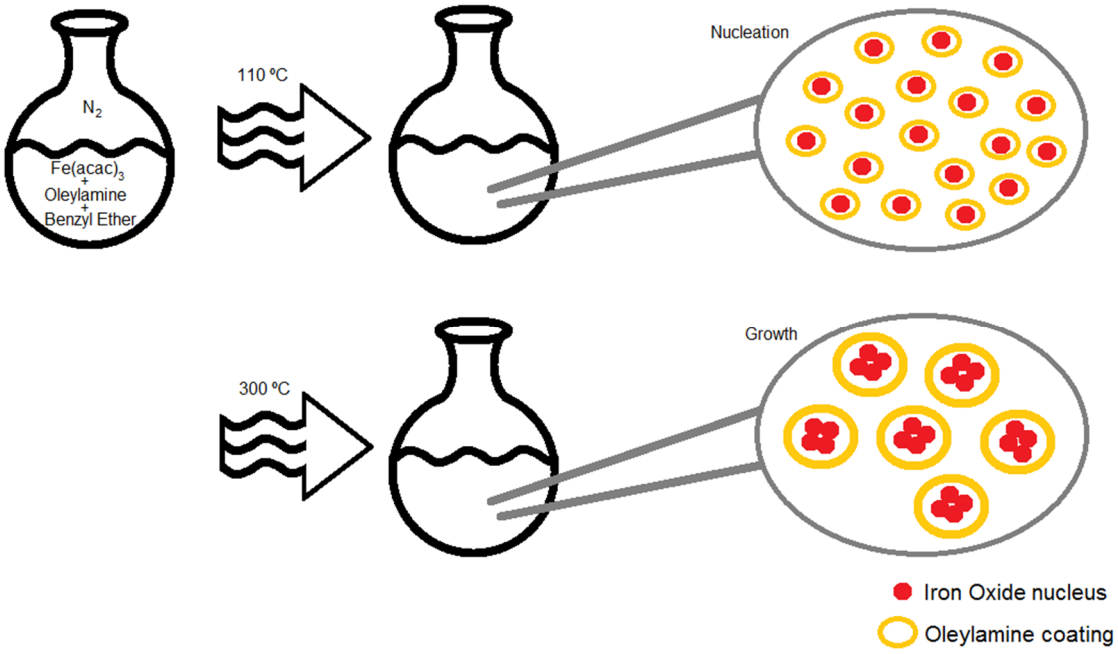


**Figure 2 – Schematic of the different phases of the reaction – details for the system under study.**

Figure 2 demonstrates the different stages explained previously but in regards to the specific reaction synthesis system that will be used in this work. Establishing a threshold at 110 ºC guaranteeing the nucleation needed for the subsequent growth of them. The growth of the nanocrystallites is obtained at a higher threshold of 300 ºC. In this phase, it is believed that the nucleation cores aggregate to form a nanostructured iron oxide in the form of round maghemite/magnetite nanoparticles.

## 2.4. Amazonian oleoresins

Natural polymers have been part of the world ever since earth had the first spark of life. Modern societies were built by what nature has given us and as well as what we could build from its raw materials. As we reach the second half of the 20$^{th}$ century, the fast development of petrochemical industries pushed organic chemistry into a new era of polymeric structures made from abundantly available fossil fuels. This new surge of macromolecules boosted the appearance of new and accessible materials that completely reshaped humankind. Thus, the “plastic age” began [11].

Synthetic polymers gave humanity an improvement in terms of wellbeing. But everything has a cost. Ecological problems arisen due to the almost non-degradability of these man-made polymers. Having a fossil fuel origin aggravates even further the bad effect it has on climate and ultimately in the big ecosphere we all live in. In order to answer to a more environmentally aware society, funds have been allocated towards research of polymers that are made from renewable resources [11].

One of the greatest renewable resources of our planet resides in its forests, the *lungs* of planet Earth. Our study will focus specifically in the Amazon rainforest. It is considered one of the greatest sources of biodiversity due to its numerous species of flora and fauna that inhabit inside it. This enormous dormant potential makes it a huge desirable site for research to develop. Unique characteristics from certain oleoresins and extracts from local plants have raised the attention of pharmaceuticals interested in developing new and more effective medicine. Most recently, oleoresins and ointments used by local indigenous people to treat certain diseases are being researched to prove/deny scientifically its effect.

Since we are aware of the immense biodiversity of the Amazon rainforest, we will focus on only two types of trees: *Copaiba* (*Copaifera spp.*) and *Andiroba* (*Carapa guianensis*).

### 2.4.1. Copaiba

*Copaiba* is the name given by Amazonian forest people to the *Copaifera* trees. Covering more than 72 different species, *Copaiba* trees are known to produce high levels of volatile sesquiterpenes. These molecules not only make a more free flowing resin as well as contribute for the resistance of the tree against microbial attacks [12].

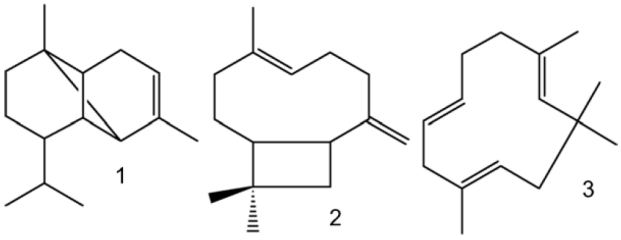


**Figure 3 - Chemical structures of (1) α-copaene, (2) β-caryophillene and (3) α-humulene, found in *Copaiba*'s oil [13].**

The main constituent of the volatile sesquiterpenes is β-caryophillene – figure 3. This sesquiterpene is a bi-cyclic hydrocarbon found in several other plants like the pine tree. Other sesquiterpenes that can be found in copaiba's oleoresin are α-copaene and α-humulene – figure 3. These terpenes have awakened a growing interest recently and studies have been made that show their high potential as anti-inflammatory, anti-allergic and antimicrobial. More specifically, β-caryophillene has also shown great potential as antioxidant and anti-carcinogenic [13].

### 2.4.2. Andiroba

*Andiroba* is the common name associated with *Carapa guianensis*. It's a medium-sized canopy tree found in the northern Amazon region in Brazil. Indigenous people of that area have been using the oleoresin extracted from *Andiroba* as an insect repellent, a reliever of muscle aches and rheumatism, and as in part of cough syrup preparations [14].

This traditional medicinal use led to studies involving the ethnopharmacological significance of this plant. It shows high potential for wound healing, treatment of arthritis, throat inflammation, diabetes, ear infection and even uterine cancer. The high therapeutic potential of this plant has been recognized to be connected to its content in tetranortriterpenoids: methyl angolensate, gedunin, 7-oxo-7-deacetoxy-gedunin and 6α-acetoxigedunin – figure 4 [15].

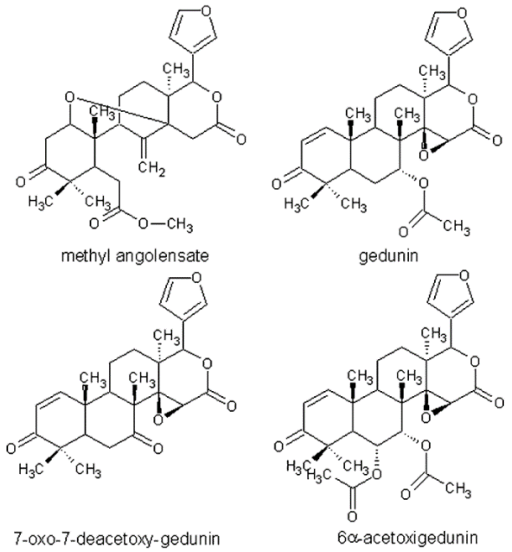


**Figure 4 - Tetranortriterpenoids found in *Andiroba*'s oleoresin [15].**

## 2.5. Characterization Techniques

### 2.5.1. Mössbauer Spectroscopy

In 1957, the German physicist Rudolf Mössbauer discovered the recoil-free nuclear absorption phenomenon. Such discovery was later named after him and currently known as the Mössbauer effect. It also awarded him the Nobel Prize of Physics in 1961 [16]. The Mössbauer effect is a phenomenon of resonant absorption of gamma rays, without recoil of the nucleus.

Mössbauer effect only occurs in solid-state when the nucleus of the sample is fixed so rigidly in the crystal lattice that recoil-free gamma-ray resonance absorption takes place. Thus, it's only observable for a certain number of elements. Solutions can be studied by examining the solids obtained after freezing them [16].

When studying the magnetism of iron, $^{57}$Fe Mössbauer spectroscopy is the ideal technique for this task. It is non-destructive, reliable, offers high resolution of charge state, ordering temperature and magnetic moment direction [17].

This method of spectroscopy applied to study Fe atoms consists of having a source containing $^{57}$Co nuclei which decays by electron capture to an excited state of $^{57}$Fe. Subsequently it decays to a ground state of $^{57}$Fe emitting the desired gamma-ray in the process. It is this gamma-ray that can excite a transition in the sample being studied if it is absorbed resonantly [6]. In figure 5 it's schematically explained how this method can be used to obtain a Mössbauer spectra.

In transmission geometry, what we obtain from a Mössbauer measurement is a plot of relative absorption against the velocity of the source having the absorber in fixed position. The movement of the source has the aim of, by Doppler effect, vary the energy emitted by the Mössbauer gamma ray (14.4 keV for $^{57}$Fe).

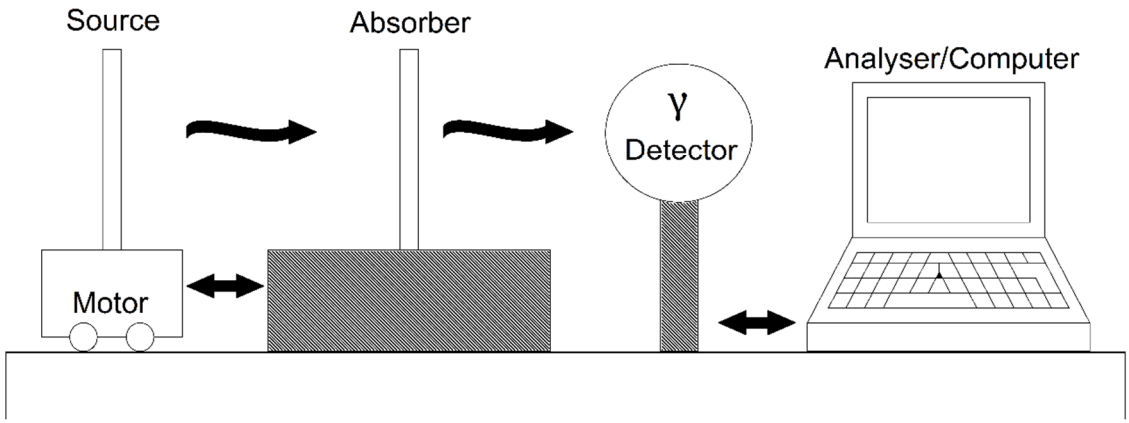


**Figure 5 – Experimental assembly representation of Mössbauer spectroscopy in transmission geometry.**

If the gamma-ray excites a transition in the sample then the computer records that interaction as a point. After finalizing the data acquisition a lorentzian approximation is performed to the scattered data obtaining a Mössbauer spectra.

In table 3, the types of interactions the gamma-rays have with the samples being studied are described. Depending on the type of sample being studied some interactions will be more evident than others.

**Table 3 - Description of hyperfine interactions that occur in Mössbauer Spectroscopy [8].**

| Name | Description | Illustration of interaction |
|---|---|---|
| **Isomer shift (δ)** | Energy difference in the s-electron environment between the source and absorber produces a shift in the resonance energy of the transition. This shifts the whole spectrum positively or negatively depending upon the s-electron density. |   |
| **Quadrupole splitting ($\Delta E_Q$)** | Splitting of energy levels caused by interaction between the nuclear quadrupolar moment and an electric field gradient at the nucleus. |   |
| **Hyperfine magnetic field (H)** | Interaction of the dipole moment of the nucleus and the hyperfine magnetic field causes a splitting of the nuclear energy levels. | 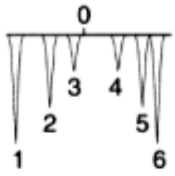  |

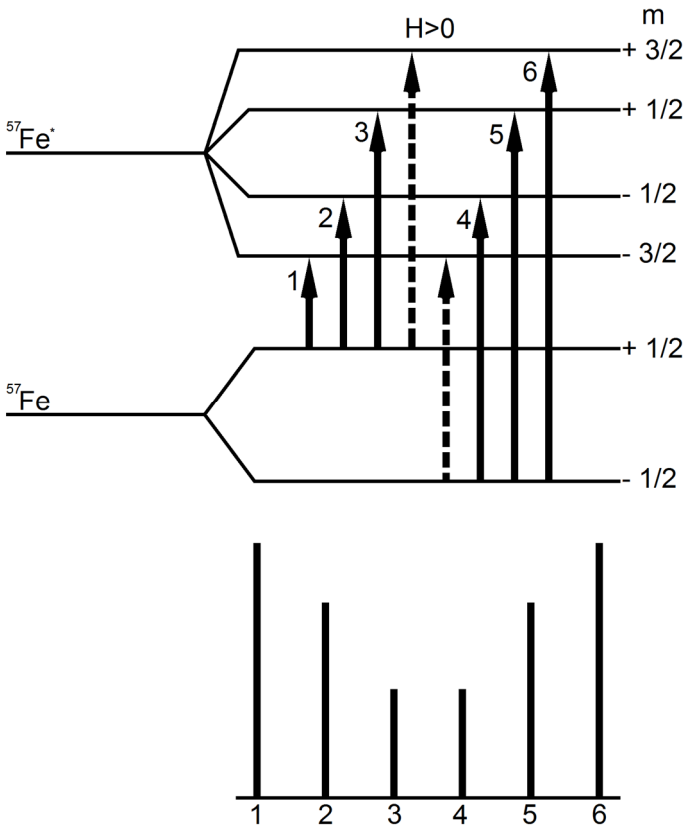


**Figure 6 – Six lines of a typical spectrum of metallic iron.**

The number of peaks obtained in a Mössbauer spectra is related to the solid state transitions allowed between $^{57}Fe$ and its excited state $^{57}Fe^*$ as shown in figure 6.

Depending of the crystal arrangement of the sample, more than one absorption line as a function of source velocity can be observed. Each line central position is given in function of an arbitrary origin, which is frequently the centre of the spectrum corresponding to a sample of metallic iron measured at room temperature.

The spectrum characteristics, the hyperfine interactions that can be obtained depend on the nature of the studied sample (perturbations made by the environment of Mössbauer nucleus). At the origin of each hyperfine interaction there is a coupling between the resonant nucleus and the electrons surrounding them. The parameters obtained in the fitting of spectra are the hyperfine parameters determined from the profile of the spectra, as described in table 3.

It should be noted that when the size of the grains is too small, the superparamagnetic character (relaxation effect of the magnetic state) of iron is shown by the presence of a single line centred near zero nm/s.

The reason is that magnetic properties of nanoparticles may differ from those of bulk materials. The most dramatic effect of a small particle size is that the magnetization direction is not stable but fluctuates.

In practice, a sample of magnetic nanoparticles will normally show a distribution of particle sizes and there is also a distribution of magnetic anisotropy constants. Because of the exponential dependence of the relaxation time on the energy barrier, $kV$, this results in a very broad distribution of relaxation times and Mössbauer spectra may have sextets and doublets or singlets due to different relaxation times of different size of particles. Often, the broad components due to same size of particles have a low relative area such that they are barely visible in the spectra. The area ratio of the sextets and doublets or singlets varies with temperature because of the temperature dependence of the relaxation time.

The blocking temperature is not uniquely defined. In Mössbauer spectroscopy, the study of samples with a broad distribution of relaxation times show that average blocking temperature is commonly defined as the temperature where half of the spectral area is in a sextet and half of it is in a singlet or a doublet form.

### 2.5.2. X-Ray Diffraction (XRD)

X-ray diffraction is still one of the most reliable methods used to identify iron oxides crystalline phases since it is based on the long range order of the atoms. It consists of interacting electromagnetic radiation with the atoms of the sample. The crystal lattice constituted by those atoms diffract x-ray in different directions depending on how the x-ray beam interacts with the crystal planes of the solid phase, ultimately resulting in different diffraction patterns (diffractograms). These patterns are sort of a very specific crystallographic print that can be matched and compared with reference ones from the existing databases [8].

The electromagnetic radiation that interacts with the sample has its characteristic wavelength ($\lambda$) that depends on its source, and it also has an oriented angle of incidence ($\theta$), at which it hits the sample. For certain values of

$\theta$, the radiation of the source interferes constructively with defined sets of parallel planes of the crystal, with interplanar spacing (*d)* enhancing the intensity of the diffracted radiation. Bragg's equation correlates all those parameters:

$$n\,\lambda = 2\,d_{hkl}\sin\theta \qquad (3)$$

*n* is an integer indicating the order of diffraction and $d_{hkl}$ is the lattice spacing of the plane family (*hkl*) of the sample. Every crystalline phase has its own set of interplanar spacing ($d_{hkl}$) and intensities, allowing the identification of the phase under study [8]. In the condition of Bragg's law, the incident beam and the diffracted beam are symmetric in relation to the normal of the diffracting surface, as shown in figure 7.

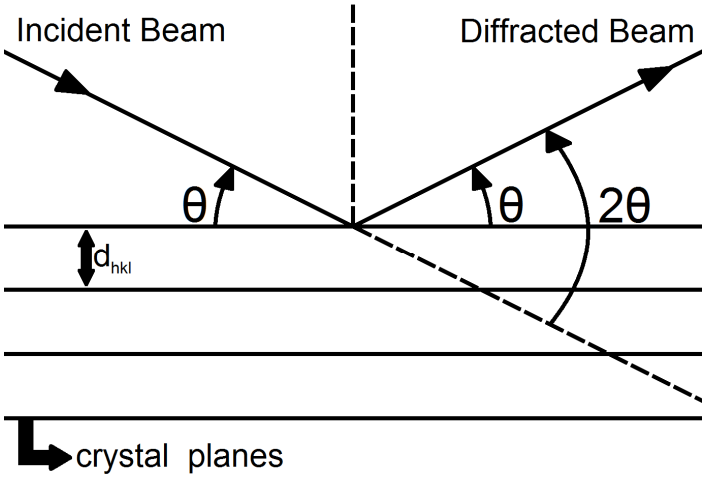


**Figure 7 – Schematic representation of x-ray diffraction phenomenon (Bragg's law).**

The intensities obtained for 2$\theta$ angles correspond to the diffraction of the incident beam by a set of crystal planes with the same interplanar spacing. Each one identified with their own Miller indices *hkl*. These intensities are seen in the diffraction peaks of the obtained patterns. Each diffraction peak is characterized by 3 features: position, intensity and shape.

The position is related to the medium value of distances $d_{hkl}$, depending on the unit cell parameters. Besides the nature and composition of the diffraction volume, this position also depends of the global mechanical state.

The integrated intensity is proportional to the number of crystallites in conditions of Bragg diffraction, and is influenced by the orientation of coherent domains of diffraction.

The shape of the peaks is related to the dimension and deformation of each coherent domain.

The Full Width at Half Maximum (FWHM) of a diffraction peak results from the convolution of three distinct effects: the instrumental resolution, the size of crystallites and the degree of strain. The FWHM due to instrumental resolution, has no significance in the analysis of nanomaterials, so it can be neglected. The average size of crystallites (*D*) can be determined by the Scherrer formula:

$$\beta = \frac{\varepsilon\lambda}{D\cos\theta} \quad (4)$$

Where $\beta$ is the FWHM of the peak in terms of $2\theta$ and measured in radians, $\lambda$ the wavelength of the incident x-ray beam and $\varepsilon$ is a form factor of the crystallites. Usually an approximate value of 0.9 is assumed.

The broadening of the peaks due to the decreasing of crystallites size is explained by the decreasing of diffraction coherent domains. So, the radiation emitted by the diffracting planes according to a certain Bragg angle $\theta$, due to their small number, is not able to cancel by destructive interference the incoherent radiation coming from planes where Bragg angle is near $\theta$.

A diffractogram obtained with monochromatic radiation of a known wavelength has all the information to obtain the cell parameters of the crystal. These parameters are calculated by the quadratic formulae corresponding to the crystalline systems.

### 2.5.3. Vibrating Sample Magnetometer (VSM)

Magnetic properties like the type, strength and direction of the remnant magnetization are used to characterize different iron oxides. Magnetite and maghemite have higher magnetic susceptibility ($\chi$) than any other iron oxide, thus their presence in a sample will dominate its magnetization characteristics [8].

Simon Foner invented the vibrating sample magnetometer in 1955. Although there are several possible detection-coil arrangements, all of them are based on the same principle – Faraday's law. This law states that an electromagnetic field is generated in a coil when a change in flux linking the coil is induced.

A coil with *n* turns of cross sectional area (a) can be described as:

$$V = -na\frac{dB}{dt} \quad (5)$$

If said coil is positioned in a constant magnetic field, then:

$$B = \mu_0 H \tag{6}$$

When we introduce our sample, with a magnetization M, into the coil:

$$B = \mu_0 (H + M) \tag{7}$$

The flux changes correspond to:

$$\Delta B = \mu_0 M \tag{8}$$

If we combine the previous equations:

$$Vdt = -na\mu_0 M \tag{9}$$

Meaning that the output signal of the coil is proportional to the magnetization of the sample (*M*) but independent of the magnetic field that the sample is subjected to (*H*) [18].

In practice, the sample (contained inside a small pill) is attached to the end of a nonmagnetic rod (figure 8). The other end of the rod is fixed to a linear motor making the sample oscillate according to a desired frequency. As a result of this movement, an alternating electromagnetic field is induced in the detection coil.

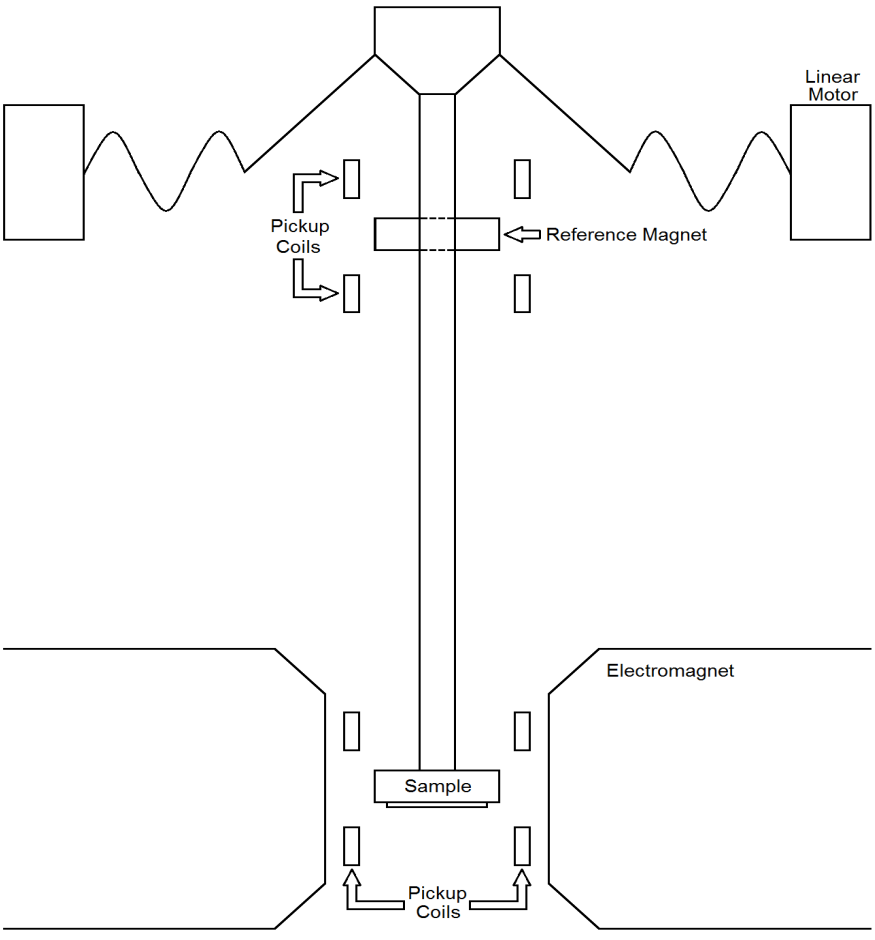


**Figure 8 - Schematic of a VSM [19].**

The alternating electromagnetic field is usually small and is therefore amplified with a lock-in amplifier. This type of amplifier is sensitive only at the frequency of vibration and must be provided with a reference signal originated from a sensor coupled to the driving system that makes the sample oscillate.

In order to keep results accurate, calibration is made with a specimen of known magnetic moment and, ideally, this specimen must have the same size, shape and similar permeability as the sample being measured.

Certain cares must be taken in account when performing this analysis. Cleanliness of the sample must be assured, because even small amounts of contaminating material can saturate the measurement of small or weakly magnetic samples. The sample must also be short, and the demagnetizing field may then be such a large fraction of the applied field that the true field is uncertain.

Being both versatile and sensitive, the VSM can be used for weakly and strongly magnetic materials [19].

### 2.5.4. Fourier Transform Infrared (FTIR) spectroscopy

Infrared spectroscopy results are based on the molecular interactions of the sample with electromagnetic radiation (photons) in the wavenumber range of 10000-33 $cm^{-1}$. These interactions induce the excitation of vibration or rotation of molecules from their ground state. Normally, they are associated with stretching deformations of interatomic bonds and bending deformations of the interbond angles. When a sample is crossed by a beam of infrared (IR) light, the sample absorbs radiation in a wavenumber frequency which is dependent on the rotational/vibrational energy levels and force constants associated with interatomic bonds [8].

As a result of how photons interact with molecules from the sample, an infrared spectrum is obtained. It is a plot of the percentage of radiation absorbed (or transmitted) versus the wavenumber frequency of the incident radiation [8].
Identification of a substance is possible because differences in the chemical structure of materials give rise to characteristic vibrations and yield unique IR spectra for each material.

### 2.5.5. Thermal Analysis

Thermal analysis methods share the same principle: heating the sample with a programed profile (usually at a constant rate (2-10$^{o}$C.min$^{-1}$)) and measuring a property of the sample (weight, temperature, volume, *etc.*) with a very precise scale. Thermal analysis methods commonly used to characterize iron oxides are thermal gravimetric analysis (TGA) and differential scanning calorimetry (DSC) [8].

TGA measures the weight of the sample versus the time/temperature while DSC measures the exchanged heat flow as a function of time/temperature. The experiments can be conducted in various atmospheric conditions, *e.g.*, vacuum, inert, oxidative or reactive. In the DSC, it is possible to obtain peaks that represent endothermic or exothermic events in the sample. These peaks normally give information about the phase changes of the sample or undergoing reactions [8].

In the case of magnetite, thermograms show two exothermic peaks corresponding to phase transformations. First, from magnetite ($Fe_3O_4$) to maghemite ($\gamma$-$Fe_2O_3$) and, second, from the resulting maghemite to hematite ($\alpha$-$Fe_2O_3$) [8].

### 2.5.6. Transmission Electron Microscopy (TEM)

Modern transmission electron microscopes (TEM) are complex machines. They are composed of very different analysers that measure the interaction between the electron beam, produced in the electron gun at the top of the instrument, with the sample, laying at the bottom of the microscope. Sensors like EELS (Electron Energy Loss Spectrometer) and EDS (Energy Dispersive x-ray Spectrometer) analysers present in TEM machines make this characterization technique go beyond than just outputting a high resolution image of a nanoscaled sample [20].

As the name implies, in TEM, one works in transmission mode so that the sample must be “transparent” to the electrons (the maximum thickness at the borders is about 100 nm).

In transmission electron microscopes, a beam of high-energy electrons is generated at the gun chamber and accelerated by an electrical potential

difference that could reach 1000 kV. The beam is then collimated by magnetic lenses and allowed to pass through a specimen under high vacuum. The resulting diffraction pattern, which consists of a transmitted beam and a number of diffracted beams can be displayed on a fluorescent screen below the specimen. The several layers of components inside a TEM are shown in figure 9.

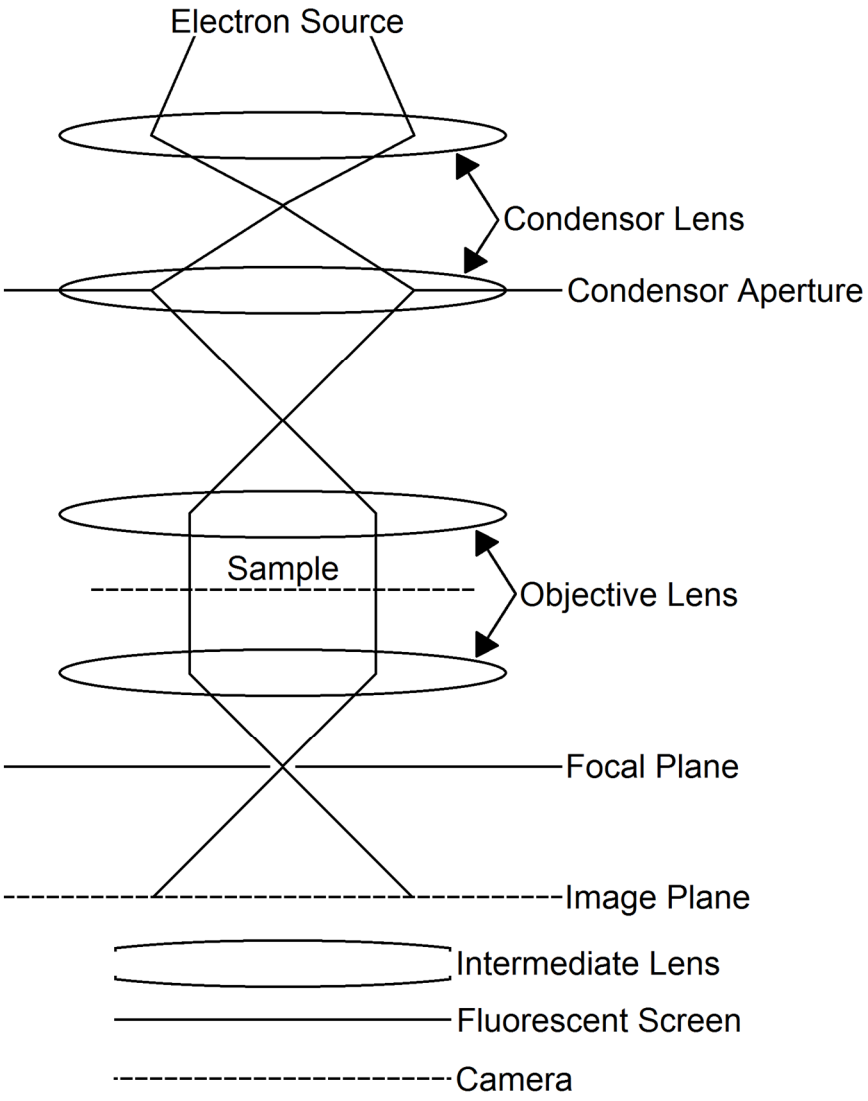


**Figure 9 – Schematic representation of the basic principle behind TEM.**

From the diffraction pattern, one can obtain the lattice spacings of the structure under consideration. Alternatively, one can use the transmitted beam or one of the diffracted beams to form a magnified image of the sample on the viewing screen.

# 3. Experimental Work

## 3.1. Materials

Iron(III) Acetylacetonate ($(Fe(C_5H_7O_2)_3)$, $Fe(acac)_3$, 97 %), Iron(II) Acetylacetonate ($(Fe(C_5H_7O_2)_2)$, $Fe(acac)_2$, 99.95%), Oleylamine ($(C_{18}H_{35}NH_2)$, 70 %), and Benzyl Ether ($(C_7H_7OC_7H_7)$, 98%) were purchased from Sigma-Aldrich. Oleic Acid ($(C_{17}H_{33}COOH)$, 85-90%) was purchased from The British Drug House. 1,2-Hexadecanediol ($(C_{16}H_{32}(OH)_2)$, >98%) was bought from Tokyo Chemical Industry. All the reagents were used without further purification.

## 3.2. Synthesis of $Fe_3O_4$ nanoparticles

Throughout the course of this thesis, $Fe_3O_4$ nanoparticles were obtained using different methodologies but with very similar experimental procedures. Furthermore, all of those methods used the same experimental assembly, outlined by figure 10. Due to the high temperature these methods achieve, reflux was always present to better condensate the volatile gases released.

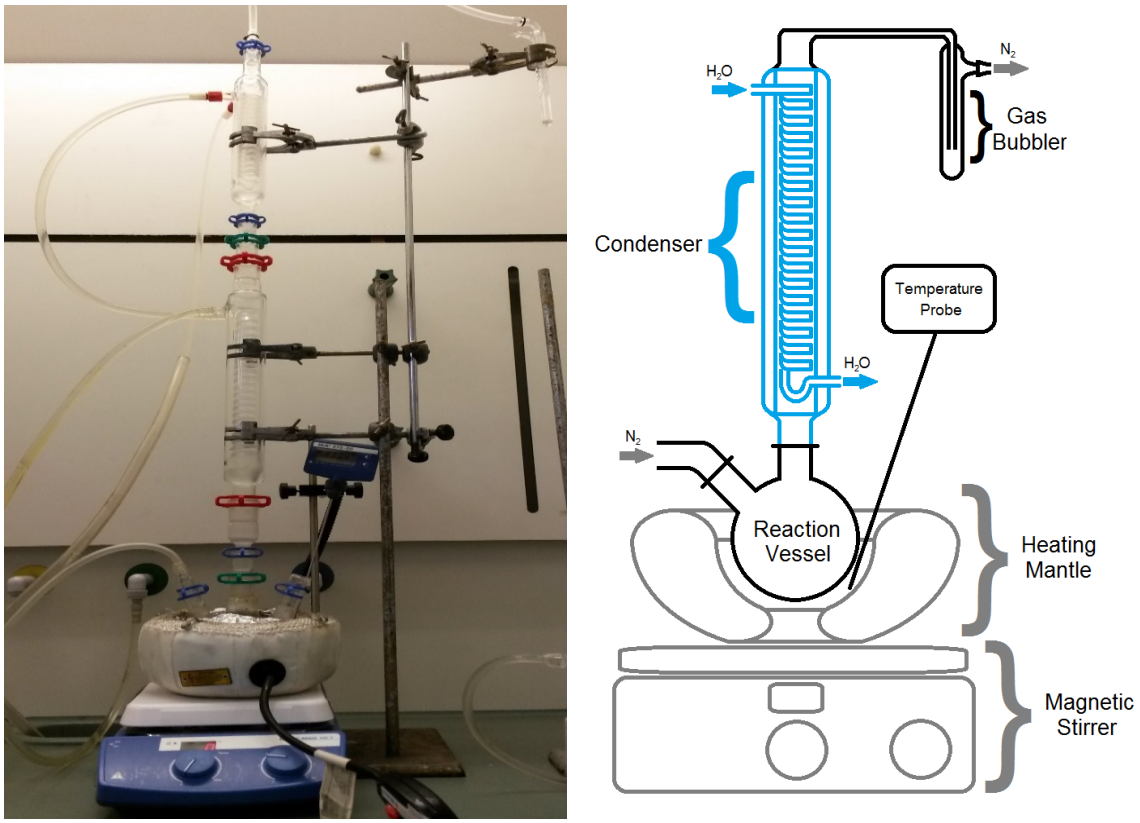


**Figure 10 - Synthesis reaction experimental assembly: real (left) and schematic (right).**

Initially, three different methods were tested: A, B and C. All of which followed their respective literature with a slight detail of being scaled down. Quantities used for method A were 1/6 of the original and methods B and C were 1/4.

### 3.2.1. Method A

For method A, 1 mmol of $Fe(acac)_3$, 4 mL of Oleylamine and 1 mL of Benzyl Ether were added into a 3 neck round-bottom flask [21]. The mixture was magnetically stirred and put under a flow of $N_2$ throughout the course of the reaction.

Two thresholds of temperature were established: the first at 110ºC during 1 hour and 15 minutes, for the formation of seeds, and another at 300ºC during 45 minutes, for the growth of nanocrystals. The first threshold was reached at a rate of 10ºC/minute. The second threshold was reached at a rate of 16ºC/minute. The obtained mixture was then let to cool down until room temperature.

### 3.2.2. Method B

Method B used 0.5 mmol of $Fe(acac)_3$, 2.5 mmol of 1,2-Hexadecanodiol, 1.5 mmol of Oleic Acid, 1.5 mmol of Oleylamine and 5 mL of Benzyl Ether [22]. The mixture was magnetically stirred and put under a flow of $N_2$ throughout the course of the reaction.

Two thresholds of temperature were applied, as before, for nucleation and growth of nanoparticles, respectively: the first at 330ºC for 30 minutes and another at 400ºC for 50 minutes. The mixture was heated, at a rate of 19ºC/minute, until the first threshold was reached. The second threshold was reached at a rate of 1.9ºC/minute. The obtained mixture was let to cool down until room temperature.

### 3.2.3. Method C

Method C used 0.5 mmol of $Fe(acac)_3$, 2.5 mmol of 1,2-Hexadecanodiol, 1.5 mmol of Oleic Acid, 1.5 mmol of Oleylamine and 5 mL of Benzyl Ether [22]. The mixture was magnetically stirred and put under a flow of $N_2$ throughout the course of the reaction.

At a rate of 2.3ºC/minute the mixture was slowly heated until the 300ºC threshold was reached. It was then maintained at this temperature for an hour. The obtained mixture was let to cool down until room temperature.

### 3.2.4. Methods AD, AE and AF

These 3 variations of method A were investigated by changing the initial quantities of $Fe^{3+}$ and $Fe^{2+}$ at the start of the reaction, in order to observe their effect in the resulting phases. This was made by changing the initial amounts of the iron acetylacetonate precursors as it is demonstrated in table 4.

**Table 4 - Ratios of $Fe(acac)_2$ and $Fe(acac)_3$ used in methods AD, AE and AF.**

| Method | Percentage of $Fe(acac)_3$ | Percentage of $Fe(acac)_2$ |
|---|---|---|
| **AD** | 95 | 5 |
| **AE** | 66 | 33 |
| **AF** | 5 | 95 |

### 3.2.5. Methods AG and D

Procedures AG and D were used in order to give a better understanding of the synthesis reaction process.

Method AG followed all the procedure described for method A, except for a change that was made on the time the first threshold was maintained. In this part of the experiment, the first threshold time of 1 hour and 15 minutes was doubled to 2 hours and 30 minutes. This change was made in order to understand the impact that this threshold has in the overall reaction and in the size of the nanoparticles.

Method D was implemented in order to understand if the Oleic Acid could substitute Oleylamine present in method A and observe the differences in the synthesis products.

1 mmol of $Fe(acac)_3$, 4 mL of Oleic Acid and 1 mL of Benzyl Ether were used, following the amounts defined in method A. The mixture was magnetically stirred and put under a flow of $N_2$ throughout the course of the reaction.

Two thresholds of temperature were established, as already described for method A: the first at 110ºC during 1 hour and 15 minutes and another at 300ºC

during 45 minutes. The first threshold was reached at a rate of 10ºC/minute. The second threshold was reached at a rate of 16ºC/minute. The obtained mixture was then let to cool down until room temperature was reached.

### 3.2.6. Purification Method

After the mixture reached room temperature, it was dispersed in ethanol and centrifuged at 7000 RPM for 10 minutes. We repeated this process several times in order to obtain a clear separation between ethanol and the nanoparticles deposited at the bottom of the falcon.

### 3.2.7. Storage Method

The obtained nanoparticles were re-dispersed in hexane and stored in the refrigerator. Hexane solvent forms a highly stable *nanofluid* solution with the synthesized nanoparticles. Because of this phenomenon, centrifugation proves to be inefficient to separate solvent from particles. As a result of this, storage in hexane was only done if the nanoparticles weren't meant to be dispersed in any other solvent.

## 3.3. Amazonian oleoresins dispersions

Amazonian oleoresins of *Copaiba* and *Andiroba* were mixed with the obtained nanoparticles in order to form a stable dispersion. After this step, the mixture was submitted to ultrasonification for 30 minutes at a low frequency. After this, the mixture was stored in the refrigerator to preserve all its qualities until further use.

## 3.4. Characterization techniques/Procedures

### 3.4.1. Mössbauer spectroscopy

During the course of this work, Mössbauer spectra were taken at room temperature (RT) and at 4.2 K in a transmission conventional spectrometer, with constant acceleration. The RT spectra were taken in the Physics Department of University of Coimbra and the 4.2 K spectra were taken in the Technical University of Munich. In the latter, the sample in the spectrometer was cooled making use of a helium closed cycle cryostat. After preparation of the samples,

they were shipped to Munich in closed flasks with argon atmosphere in order to try to prevent oxidation.

The viscous samples were put in a plastic holder with a lid in a quantity just to cover the circular bottom surface of the holder. When powder samples were measured, the quantity of sample was about 13 mg/cm$^2$. In the measurements carried out in the cryostat, the sample holder was placed horizontally (transmission geometry in a vertical support). In the case of room temperature measurements, the sample holder was placed vertically (transmission geometry in a horizontal bench) and the samples were dried in argon atmosphere to obtain a powder.

The spectra were fitted by a set of lorentzian lines determined by least squares. The isomer shifts are given relative to α-Fe measured at room temperature.

### 3.4.2. XRD

The nanoparticles that were stored in hexane couldn't be directly measured in this method due to the presence of the liquid phase. In order to analyse them properly, droplets of the solution were deposited in a microscope slide. For each droplet deposited, hexane was let to evaporate. After repeating this process for 9 mL of solution with a concentration of 3.34 mg/mL, a black oily layer would adhere to the glass. Although difficult, the deposited layer was meant to be homogenous.

The different phases present in the samples were identified by comparison of the diffraction patterns with the ones stored in PDFs (Powder Diffraction Files).

Initially, the samples, obtained throughout the course of this thesis, were analysed in a Philips PW 1050/30 diffractometer, with a radiation of Co kα (λ=0.17902 nm). Towards the end, a Bruker 8D Advance diffractometer with radiation of Cu kα (λ=0.154184 nm) was used. Both equipment belong to the Physics Department of the University of Coimbra.

The software used to refine the cell parameters were EVA and TOPAS, part of the Bruker diffractometer package.

### 3.4.3. VSM

Sample preparation for the VSM involved the production of a very small capsule that could contain the solution. It is important that the capsule has no colour so that the pigments will not disturb the magnetic measurements. A pipette tip of 50 µl was cut to have 5 mm of diameter and 8 mm of height. The bottom was filled with melted plastic from the same pipette tip. Once the sample was poured inside, a lid was made in the same plastic and glued with a cyanoacrylate based glue. If no leaks were found, the capsule was ready to use.

The capsule was placed in a rigid tube that vibrates vertically. After determining the correct position of the sample by a scanning in the sensitive zone of the magnetic coils, the measurements then started.

The VSM used for the analysis of the samples was from Oxford Instruments and belongs to the Physics Department of the University of Aveiro.

### 3.4.4. FTIR

FTIR spectra were taken by using a FT/IR 4200 spectrometer from Jasco, using a wavenumber range of 4000-400 $cm^{-1}$ with 4 $cm^{-1}$ of resolution. For each spectra taken, a small and thin pellet was made and analysed. Each pellet consisted of 80 mg of KBr with 40 µl of the sample being studied. KBr was milled until a fine powder was obtained, and then dried in an oven at 60ºC for 2 days. After this process, 40 µl of the sample were added to the KBr powder. This mixture was milled and mixed until a homogenous powder was obtained. It was then pressed to obtain a small, thin and transparent pellet.

### 3.4.5. TEM

During the course of this thesis, TEM will only be used to verify the size of the nanoparticles of the produced particles. Preparation of the samples were done according to normal procedure for this type of technique. One droplet was deposited and let dry in a Cu microgrid. Concentration of the sample was very low to assure its *electron transparency* in order to obtain a good micrograph.

The TEM used for the analysis of the samples was a Jeol JEM 1400 electron microscope belonging to IBMC in Porto.

### 3.4.6. Toxicology analysis

For the evaluation of the toxicity of the produced iron nanoparticles, tests were made by Dr. Sofia Lima at REQUINTE (Faculty of Pharmacy of University of Porto). In order to perform these tests, the nanoparticles were functionalized with PEG-PLA, which allowed them to be stable in water and therefore suitable for the toxicity trials. For this purpose, PEG-PLA-coated nanoparticles were prepared using a water-in-oil solvent technique. Briefly, 20 mg of PEG-PLA and 50 mL of nanoparticles obtained by method A (10 mg/mL in chlorophorm) in 1 mL ethyl acetate were emulsified with an aqueous solution of 2% (w/v) polyvinyl alcohol (PVA) by sonication for 60 s (VibraCell model VCX130, Sonics & Materials, Newtown, CT, USA), at 70% amplitude. The resulting emulsion was then transferred to a round-bottom flask with 10 mL 0.2% PVA in MilliQ water. For complete solvent evaporation, a rotavapor was used for 1 h at 300 hPa and 38ºC. The PEG-PLA-nanoparticles were recovered by centrifugation at 20,000 xg for 30 min at RT and washed twice with Milli-Q water. Prior to cell culture studies, the PEG-PLA-nanoparticles were re-distributed in phosphate buffer.

The cytotoxicity arrays were prepared by using caco-2 (Human epithelial colorectal adenocarcinoma) cell line cultured in Dulbecco's Modified Eagle Medium (DMEM) with Glutamax, supplemented with 10% (v/v) fetal bovine serum and 1% penicillin-streptomycin antibiotics. All reagents were supplied by GIBCO, Life Technologies (UK). Cells were maintained at 37°C in a 5% $CO_2$ humidified incubator.

To assess the viability, cells were exposed to the different formulations at designated concentrations for 24h and then incubated with MTT (0.5 mg/mL, Sigma) at 37°C for 3 h [23]. Subsequently, the medium was discarded, and the same volume of DMSO was added to dissolve the formed formazan crystals. The optical density of the supernatant was read at 570 nm using a microplate spectrophotometer (Synergy 2, Biotek, USA).

# 4. Results and Discussion

This chapter will consist of presenting and discussing the characterization of the synthesised samples by use of the techniques presented in section 2.5. All the different methods and paths taken during the experimental work will hopefully be clarified once we reach the end of this chapter.

## 4.1. Standard Mössbauer spectra of maghemite and magnetite

Standard Mössbauer spectra of maghemite and magnetite must be known before analysing the spectra obtained for the materials synthesized with the different methods. In order to draw comparisons, these references have to be taken in account.

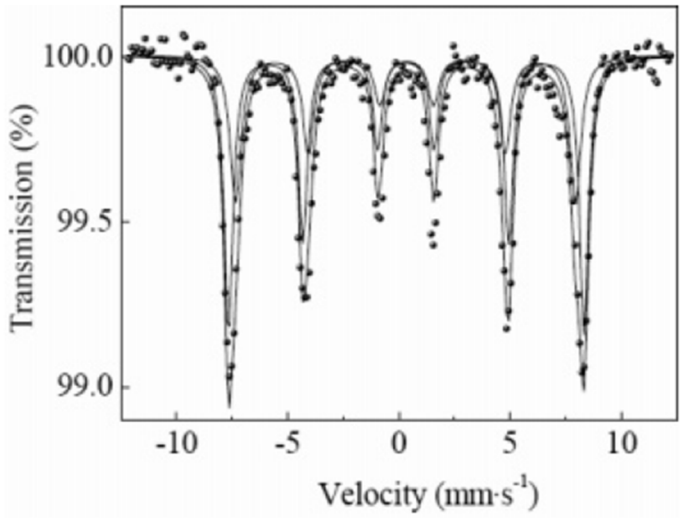


**Figure 11 – Mössbauer spectrum of pure and well crystallized maghemite taken at RT [24].**

The $^{57}$Mössbauer spectrum of maghemite at RT (figure 11) shows a magnetically split sextet with a slightly different size of the internal magnetic field: 50.2(1) T and 50.5(1) T [25].

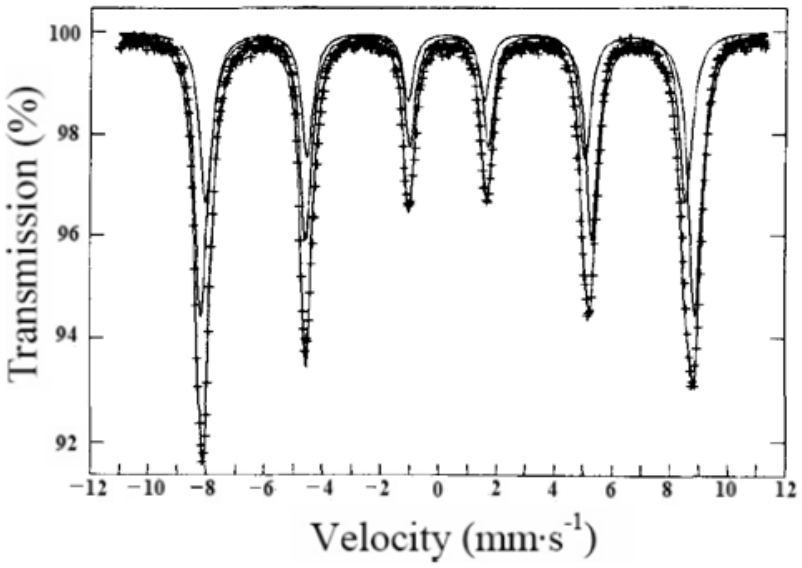


**Figure 12 - Mössbauer spectrum of pure and well crystallised maghemite taken at 8 K [26].**

Figure 12 shows a typical spectrum of pure maghemite obtained at 8 K. Of note, the asymmetry in the line depths, with the leftmost peak being narrower but deeper than the rightmost one. The spectrum can also be fitted with two sextets with internal magnetic fields of 48.0(2) T and 51.5(2) T [26].

For nanoparticles, the spectra can be very complex and dependent not only on particle size but in the type of interactions between them. Nanoparticles have superparamagnetic behaviour and their magnetic properties can differ with the size of particles.

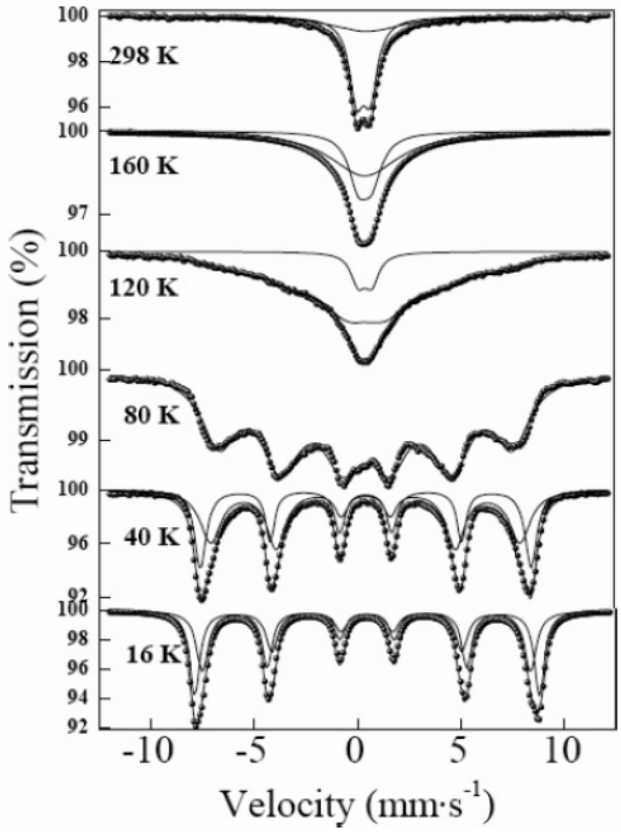


**Figure 13 - Mössbauer spectra of maghemite with 5nm particle size for different temperatures [24].**

Figure 13 presents $^{57}$Fe Mössbauer spectra of maghemite with 5 nm particle size for different temperatures. The spectrum taken at RT consists only of a central paramagnetic doublet, with parameters: IS = 0.33(1) mm/s and QS = 0.67(1) mm/s. The spectrum shows also a broad band [24].

For the spectrum taken at 16 K, the two sextets have hyperfine fields of 51.7(1) T and 49.2(1) T. Small particle sizes reduce the hyperfine fields below that of bulk material and broad resonance lines. However, direct comparison can't be done directly by using these values with the values for bulk samples given above, because the spectra were taken at different temperatures: 16 K and 8 K.

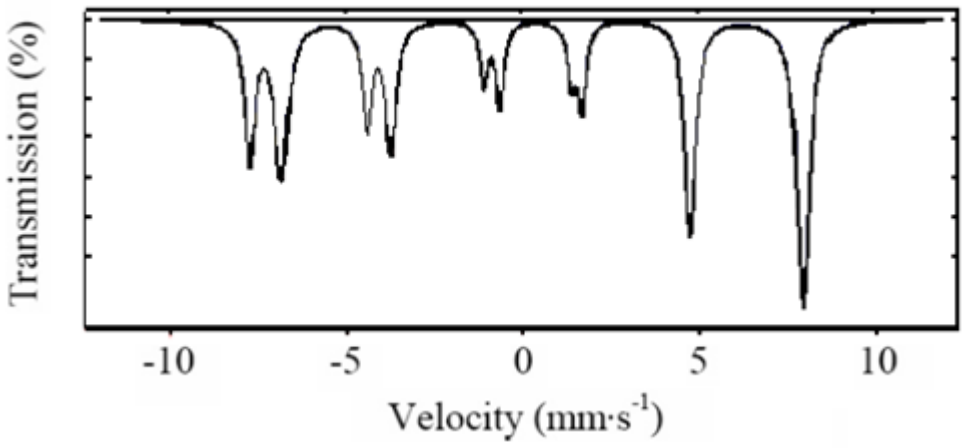


**Figure 14 – Mössbauer spectra of natural magnetite at RT [27].**

At room temperature, $^{57}Fe$ Mössbauer spectrum of magnetite typically shows two magnetic sextets, which strongly overlap (figure 14). One of the sextets arises from the iron atoms in tetrahedral sites and the other one from the iron atoms in octahedral sites. At room temperature there is a fast electron fluctuation between $Fe^{2+}$ and $Fe^{3+}$ ions in octahedral sites giving time average species with only one magnetic sextet. The magnetic hyperfine fields are 49.2(1) T and 46.0(1) T [28].

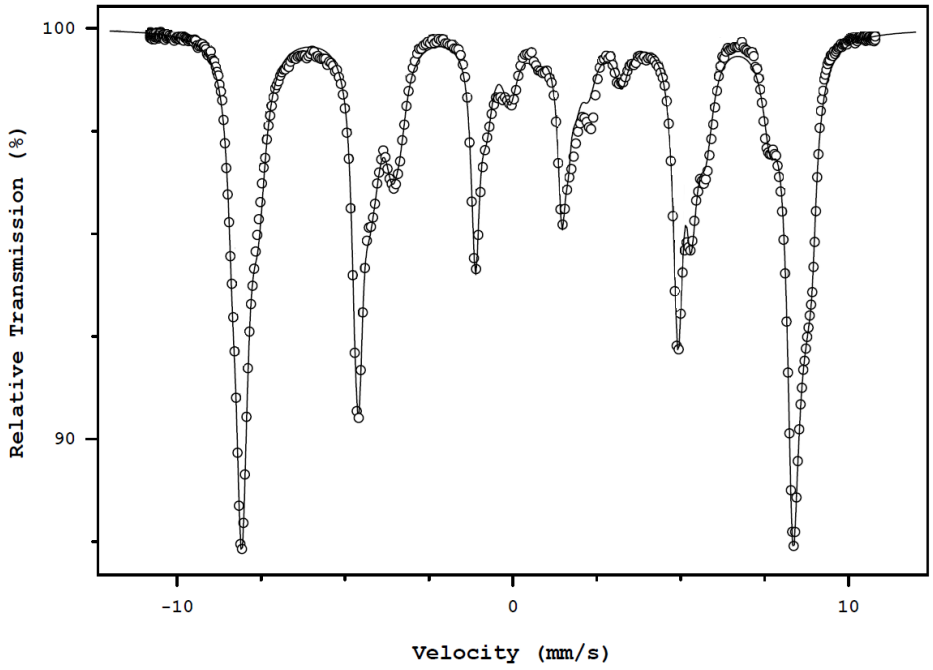


**Figure 15 – Mössbauer spectrum of natural magnetite taken at 4.2 K [29].**

At 4.2 K, the spectrum of magnetite (figure 15) is usually fitted with 5 sextets, but because of the lack of resolution, different models can be proposed. The model using 5 sextets was proposed by Berry *et al.* [30]. One component corresponds to $Fe^{3+}$ situated on the tetrahedral sites of the inverse spinel-related structure whilst the other four correspond to $Fe^{3+}$ and $Fe^{2+}$ on two non-equivalent octahedral sites. This spectrum has a very characteristic line at -3.5 mm/s that can be clearly seen.

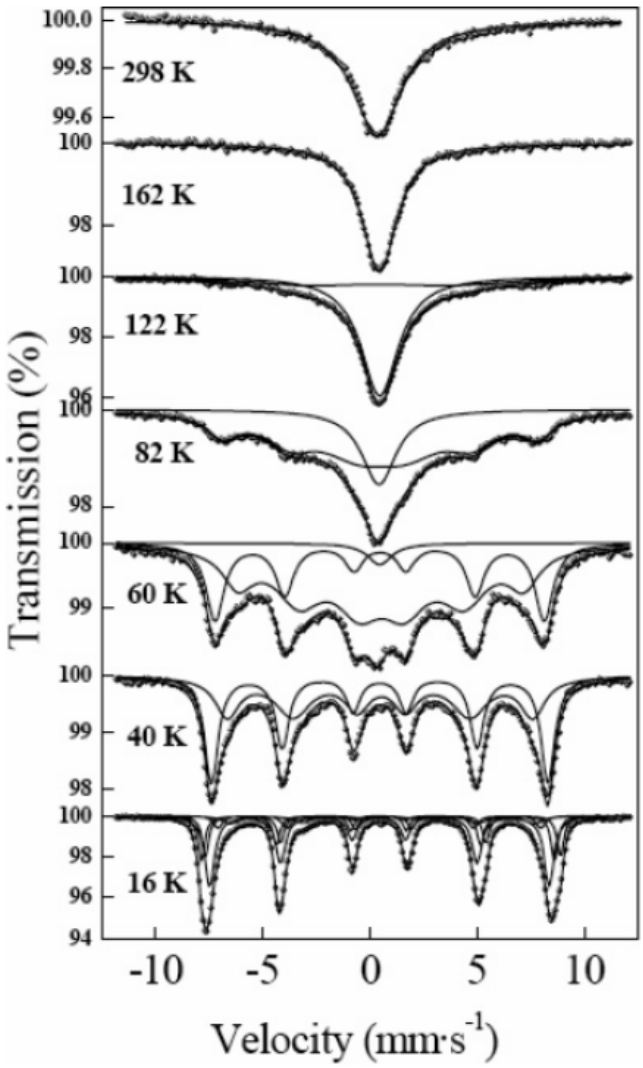


**Figure 16 - $^{57}$Fe Mössbauer spectra of magnetite with 5nm particle size in function of temperature [24].**

Figure 16 shows Mössbauer spectra recorded at different temperatures for magnetite with 5 nm particles size. The fitting of 16 K spectrum done with 5 magnetic sub-spectra gave hyperfine fields between 51.4 T and 43.9 T [24].

The spectra of nanoparticles oxides are much broaden than those of natural oxides and have lower values of hyperfine magnetic fields.

It is worth to refer that if magnetic nanoparticles are not well separated, the magnetic particle interactions may influence the magnetic dynamics. The temperature dependence of the magnetic hyperfine field is different for interacting and non-interacting nanoparticles, and the size of magnetic hyperfine field is higher for interacting nanoparticles [27].

For biomedical applications, magnetite would be preferred over maghemite because of its higher saturation magnetization and susceptibility, which means that it saturates at lower magnetic fields. However, magnetite nanoparticles with sizes below 8 nm are difficult to obtain due to the difficult stabilization against oxidation. Indeed, fine particles of magnetite oxidize to maghemite by air even at room temperature.

In this work, data of spectra are difficult to analyze and must be treated with caution, given the significant broadening of the nanocrystalline character of the samples and the existence of a particle size distribution. Furthermore, mixtures of magnetite and maghemite can be present in different proportions in each sample.

## 4.2. Comparison of the nanoparticles obtained from methods A, B and C

We will now focus in the starting methods: A, B and C. Methods A and C followed the standard procedures described in their respective literature. As for method B, this followed our own interpretation of method C. These were the methods initially tested at the beginning of this work. Since one of our goals, for the next step, was to improve or have a better insight into the process, only one synthesis method was chosen among these to pursuit that objective. The criteria for the selection were mainly the obtained phase(s) and particle size, but the cost was also considered. We will now present and discuss the characterization results obtained for samples prepared by methods A, B and C.

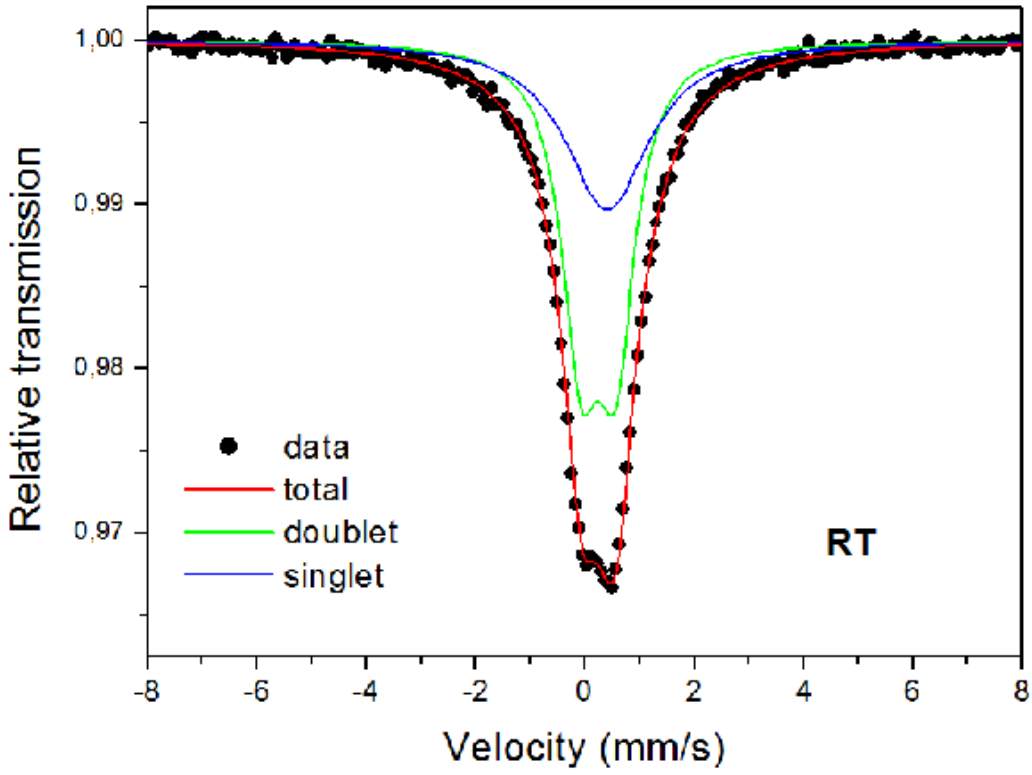


**Figure 17 - Mössbauer spectra of the sample synthesized by method A, taken at RT.**

The room temperature spectrum taken of sample A (figure 17) was fitted with a doublet and a singlet which shows the presence of small particles and superparamagnetic relaxation. The hyperfine parameters obtained by the fitting procedure are shown in table 5.

**Table 5 - Mössbauer parameters obtained by the fitting to spectrum of sample A, taken at RT (figure 17).**

| IS (mm/s) | QS (mm/s) | FHWM (mm/s) | % |
|---|---|---|---|
| 0.368(1) | 0.632(2) | 0.84(1) | 60.2 |
| 0.533(1) | - | 1.86(1) | 39.8 |

The values obtained for the doublet are consistent with the ones obtained by Roca *et al.* [24] from the spectrum at T=298 K for maghemite with 5nm particle size (figure 13).

Mössbauer spectra taken at room temperature for other samples were not obtainable, most probably because of broad distribution of particle sizes of nanoparticles yielding also a distribution of magnetic anisotropy constants.

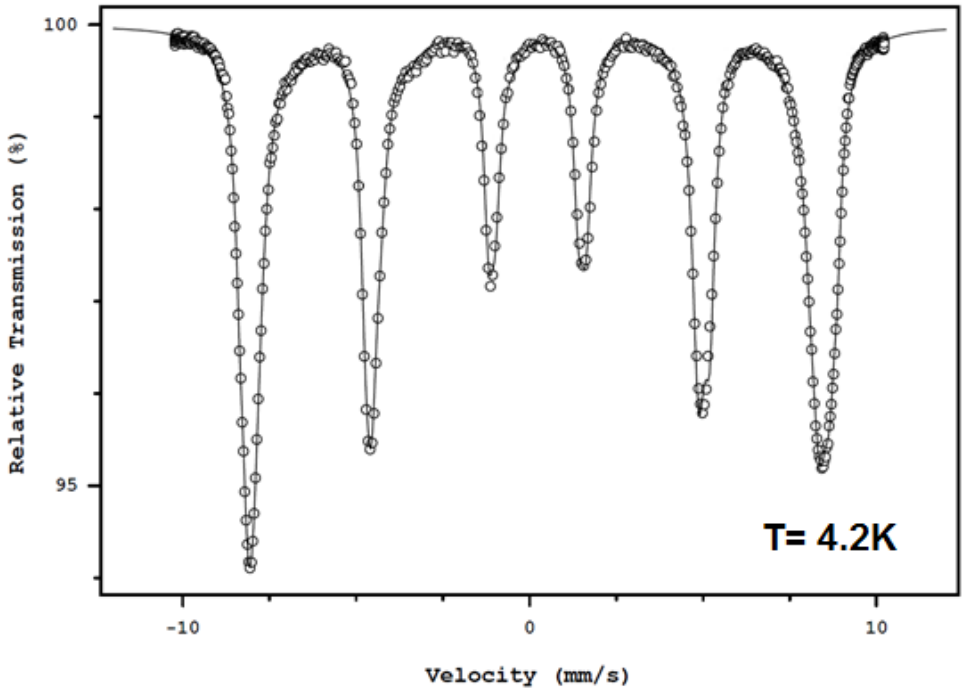


**Figure 18 – Mössbauer spectrum, at T=4.2 K, of the sample synthesized by method A.**

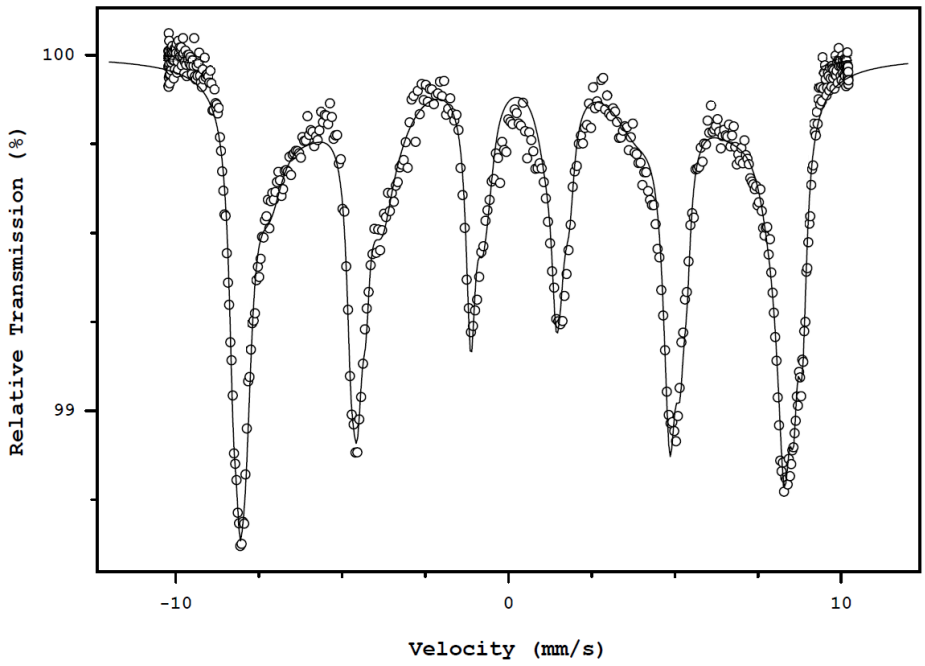


**Figure 19 – Mössbauer spectrum, at T=4.2 K, for the sample synthesised by method B.**

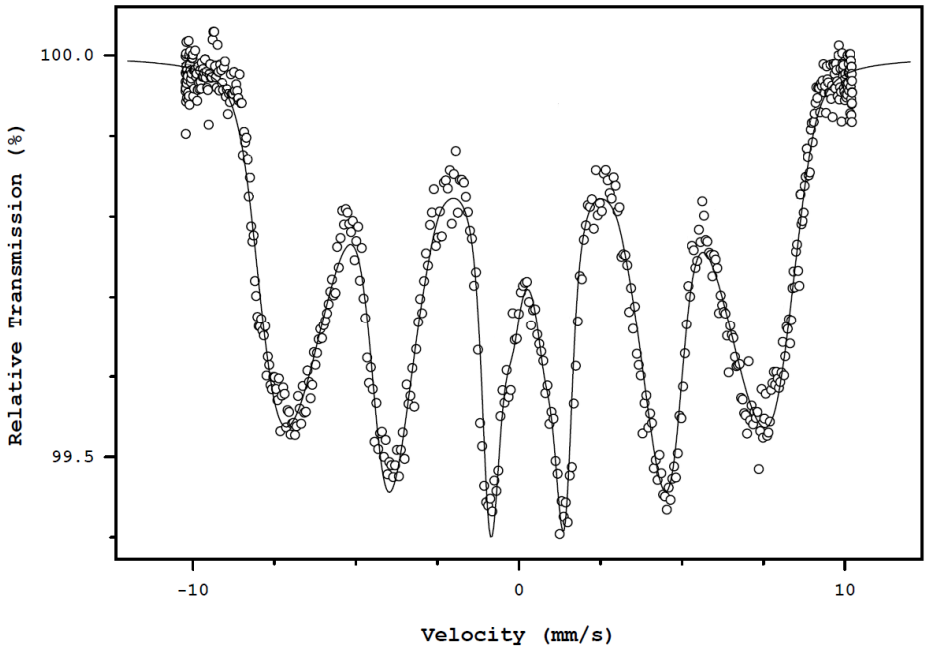


**Figure 20 – Mössbauer spectrum, at T=4.2 K, for the sample synthesised by method C.**

The analysis of the Mössbauer spectra at 4.2 K, obtained for the samples of the 3 methods denotes a major difference between methods A (figure 18) and B (figure 19) compared to method C (figure 20). We can observe in this latter method a huge relaxation effect in the corresponding spectrum, not typical at this temperature for iron oxides. This kind of relaxation is not supposed to be seen at this low temperature. This might indicate that the particles produced in this method can be maghemite or magnetite but with a size range below 5 nm. Contrasting to this, samples of methods A and B show hyperfine interactions typical of maghemite. Although maghemite is the main phase present, magnetite also exists but in a lower amount. The very characteristic line of magnetite at -3.5 mm/s can be observed in both spectra. Although the lines are very broad, method B appears to lead to a slightly higher content of magnetite than method A.

Average magnetic hyperfine fields of spectra taken at 4.2 K for samples prepared from methods A and B (figures 18 and 19) are about 49.1(3) T and 48.6(3) T, respectively.

XRD characterization of these samples was performed in order to calculate their lattice parameter and size of crystallites. Unfortunately, no results for this characterization were obtained for the sample of method C, since all data

acquisitions failed to succeed. It was assumed that this was due to very low yield of the iron oxide nanoparticles produced from this method as well as a very small crystallite size.

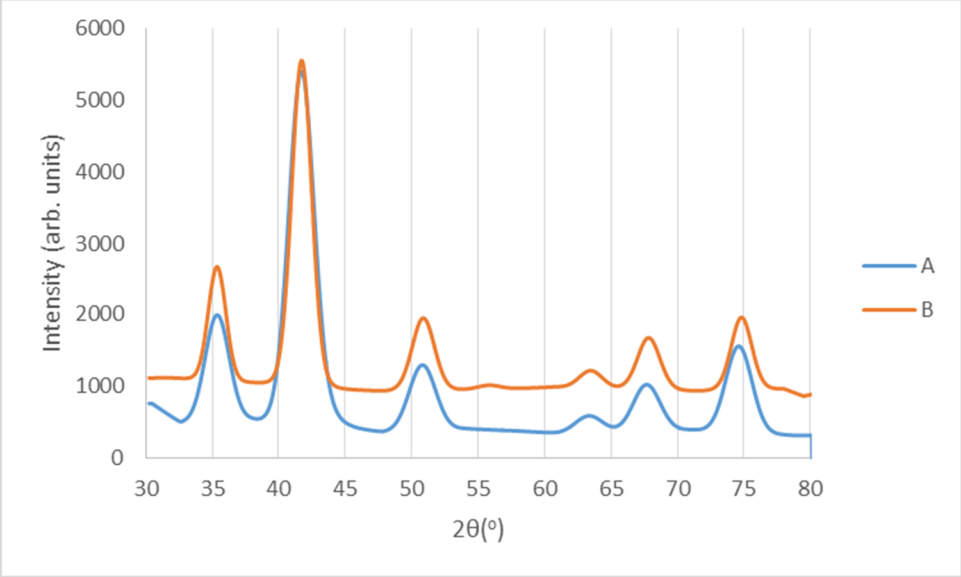


**Figure 21 – Difractograms obtained for samples produced by method A and method B.**

Figure 21 depicts how similar both diffractograms are. Both methods A and B yield nano-sized particles, so the diffractograms have very broad lines. It appears to exist no difference between the samples of both methods, but the calculated lattice parameter is slightly different. The lattice parameter value for method A is $a$=0.8369(3) nm and for method B is $a$=0.8348(3) nm. Method A result is in between the reference value for magnetite of $a$=0.8396 nm and the value for reference maghemite of $a$=0.8347 nm. The result for method B is clearly in agreement with the reference value of maghemite. Crystallite sizes ($D$) were identical for both methods, 4.5 nm.

According to the XRD characterization, both methods A and B appear to result in a mixture of both maghemite and magnetite. The closer approximation that method A has to the reference value of magnetite suggests that this method has a higher concentration of magnetite than method B. Thus, contradicting what was concluded by Mössbauer spectroscopy.

Further comparison of methods A and B was needed. The used procedures diverged slightly in terms of reactants. This made us believe that the nanoparticle

coating might be affected by the presence of extra reactants in the synthesis reaction mixture. Method A had Oleylamine to act as both reducing agent and as surfactant to form the nucleation micelles. On the other hand, method B had 1,2-Hexadecanodiol as a reducing agent and Oleic Acid along with Oleylamine to stabilize the reaction.

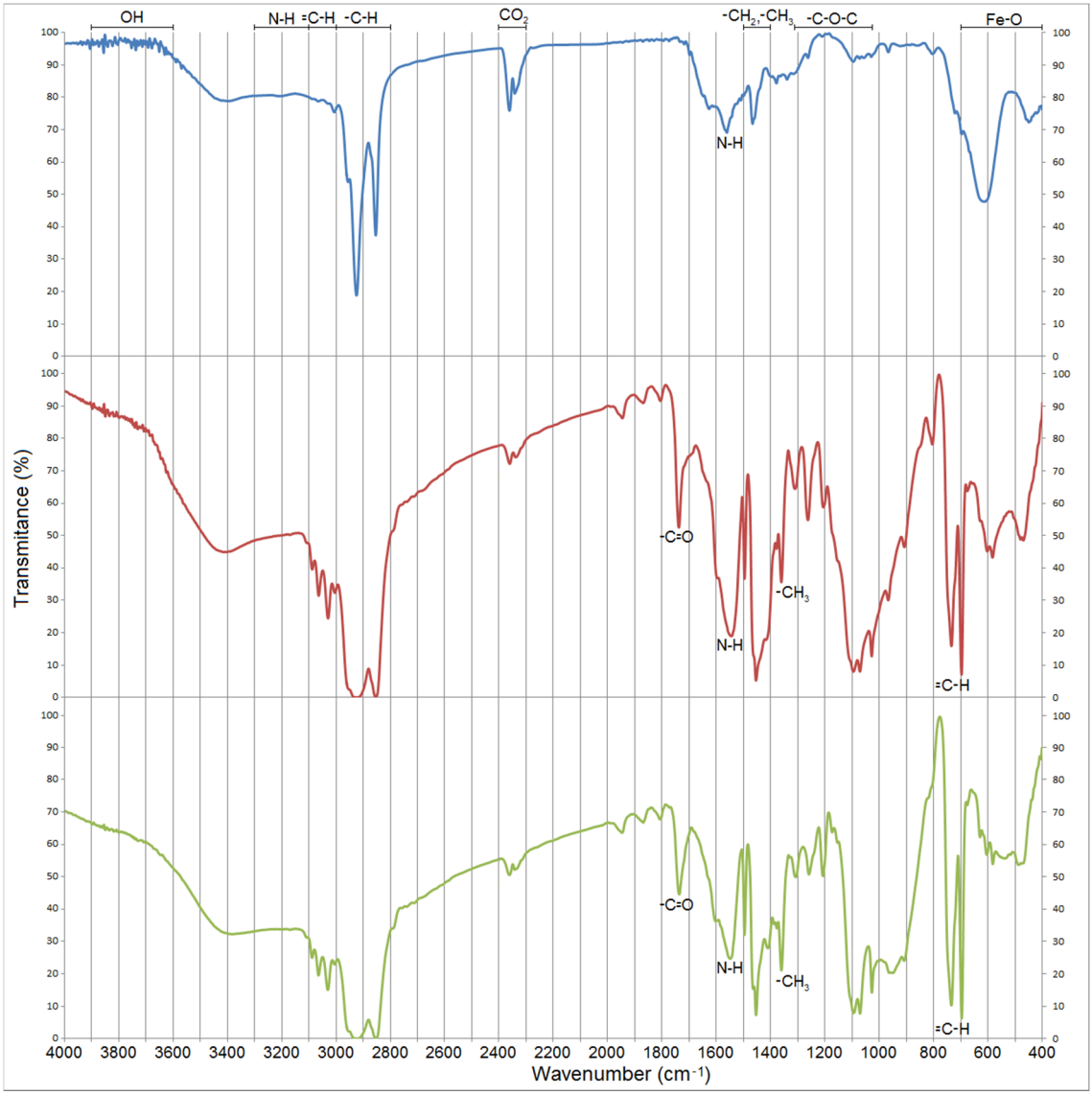


**Figure 22 - FTIR spectra obtained for the samples of method A (blue), method B (red) and method C (green).**

FTIR analysis was performed (figure 22) in order to better understand the chemical structure of the coating in the synthesized samples of methods A, B and C. The spectra baseline hardly ever recovers back after achieving a peak, which strongly confirms the amine presence in the samples, originated from Oleylamine.

Spectra from samples of method B and method C distinguish themselves from the spectrum obtained for the sample of method A due to the presence of characteristic carboxylic vibrations (1735 $cm^{-1}$), due to Oleic Acid, and an overwhelming presence of Benzyl Ether (3100-3000 $cm^{-1}$, 2000-1800 $cm^{-1}$ and 1300-1020 $cm^{-1}$) dominates great part of the spectra. All the characteristic vibrations from these compounds often create peaks of higher intensity or slight deviations from where those peaks were expected to be. Of note, the Fe-O bond at 445 $cm^{-1}$ suffers a more visible deformation for methods B and C, than for method A.

In method A, although Benzyl Ether was used, the IR spectra hardly suggests the presence of this compound contrary to what is seen in spectra from methods B and C. This leads us to conclude that the coating in method A is rather simple and only being composed of Oleylamine.

However, methods B and C have a more complex coating. IR spectra suggests an interaction between Oleic Acid, Oleylamine and Benzyl Ether to form the nanoparticles' coating. Thus, the presence of Oleic Acid seems to favour the anchoring of the Benzyl Ether molecules in the coating.

By this point, method C was abandoned due to the found difficulties and because no results revealed promising of obtaining high quality superparamagnetic iron oxide nanoparticles.

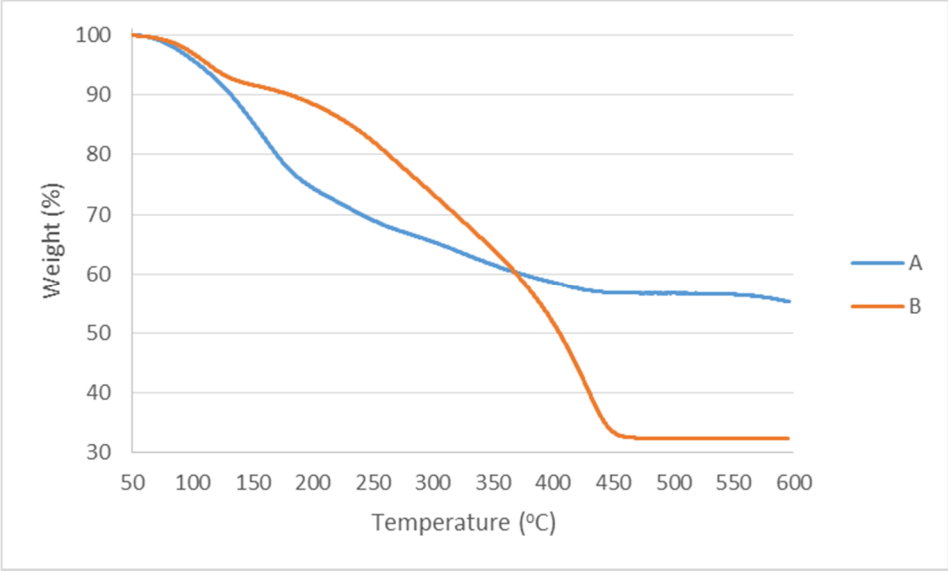


**Figure 23 – Thermograms of sample of method A (blue) and sample of method B (orange).**

Figure 23 presents the thermograms showing the difference between ratios of coating to nanoparticles for methods A and B. This becomes clearer upon further analysis of the residual weight percentage of the samples, indicating that method A has a ratio of 45% coating to 55% nanoparticles, contrasting with the ratio obtained for method B of 67% coating to 33% nanoparticles. These results improved our understanding of the used methods. When only Oleylamine is being used, a single molecule can either act as a reducing agent or as a stabilizing agent and this compound will be the coating of nanoparticles. When 1,2-Hexadecanodiol is acting as a reducing agent, more molecules of Oleylamine and Oleic Acid can be channelled to act only as stabilizing agents. This makes us believe that if each reactant is mainly performing only one role in the reaction, a more compact coating will result, as the stabilizing agents only have the role of creating micelles for particles to nucleate.

Both method A and method B yielded nano-sized particles. TEM analysis was performed in order to accurately measure the specific size of the produced nanoparticles.

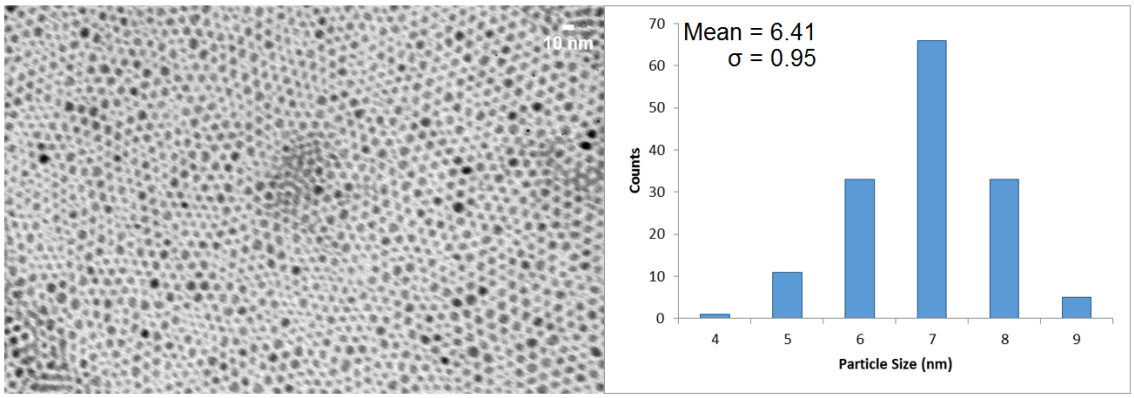


**Figure 24 – TEM image and respective size distribution calculation for the sample of method A.**

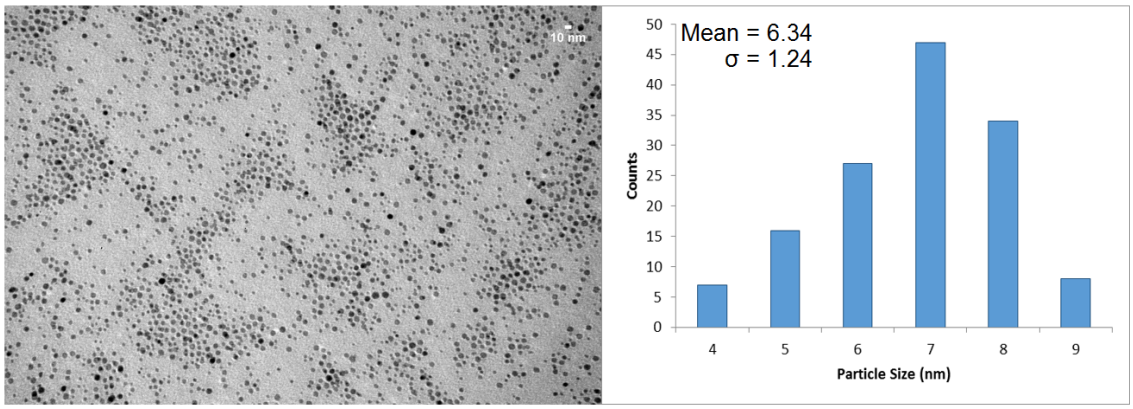


**Figure 25 – TEM image and respective size distribution calculation for the sample of method B.**

As can be observed in figures 24 and 25, both methods have very similar mean size distributions values: 6.41 nm for method A and 6.34 nm for method B. Of note, the slightly narrower size distribution for method A in comparison with method B, given by the standard deviation values of 0.95 and 1.24, respectively.

From an economical point of view, samples prepared by method B are almost 12 times more expensive than samples prepared by method A. One milligram of nanoparticles cost €0.006 to produce by method A, contrasting with €0.07 in production costs for method B.

From the previous discussion, method A was considered the more suitable method to pursue this work, in order to further study and improve the synthesis. The obtained results proved that this method led to the more promising product. The economic factor of having less and more affordable reactants also was considered.

## 4.3. Comparison of nanoparticles obtained from methods AD, AE and AF

Based on method A, methods AD, AE and AF were developed. As previously explained in the experimental work, these methods were created to study the impact of the initial concentrations of $Fe^{2+}$ and $Fe^{3+}$ precursors in the synthesis product.

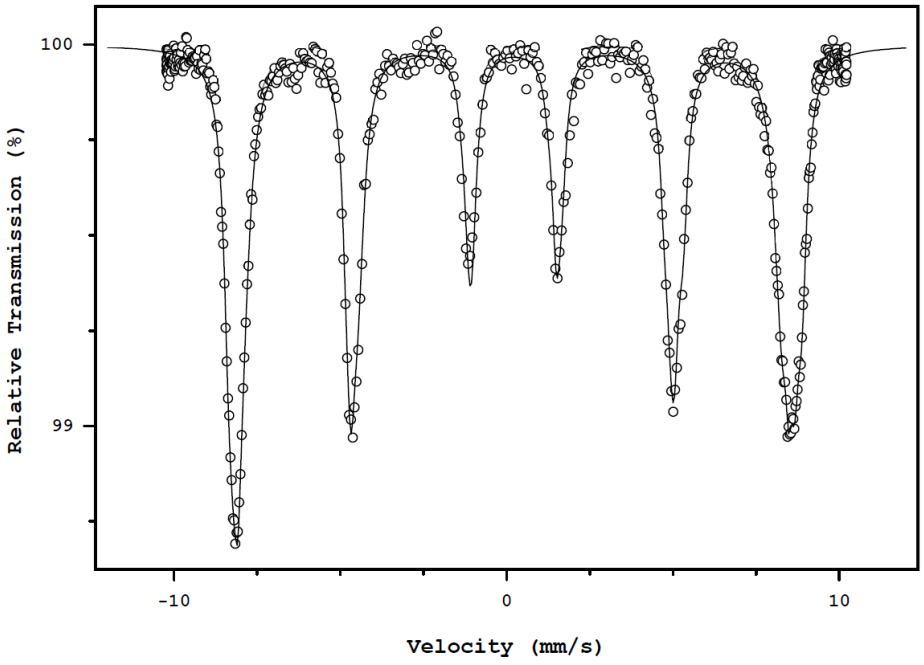


**Figure 26 – Mössbauer spectrum of the sample obtained by method AD, taken at 4.2 K.**

Mössbauer spectrum of a sample obtained by method AD (figure 26) didn't show the characteristic peak at -3.5 mm/s like it showed for the sample of method A (figure 18). The spectrum produced from a sample of method AD is similar to a maghemite spectrum, having no signs of magnetite being present. This absence leads us to believe that a mere 1% exchange between $Fe^{3+}$ and $Fe^{2+}$ can affect the ratio of magnetite to maghemite content of the nanoparticles produced. Moreover, this exchange does not favour the production of a higher magnetite yield, as could initially be expected since magnetite has some iron atoms in a 2+ oxidation state

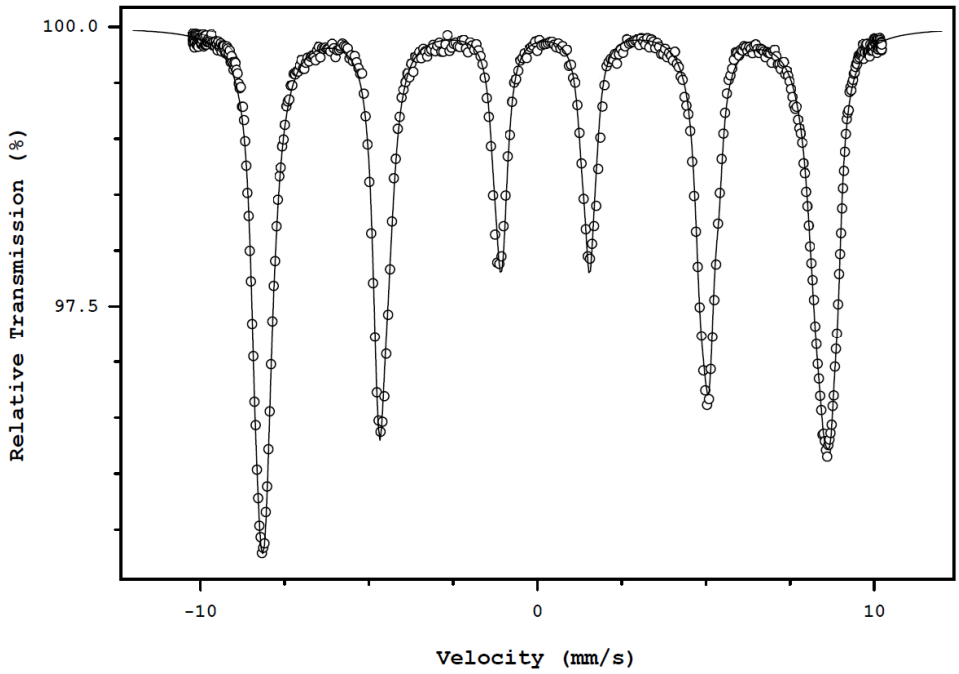


**Figure 27 – Mössbauer spectrum of a sample produced by method AE, taken at 4.2 K.**

The spectrum obtained for a sample obtained by method AE (figure 27) showed no signals of change from the previous results obtained for method AD. Since for this method, theoretical $Fe^{3+}$:$Fe^{2+}$ ratio of magnetite was used, in order to mimic the natural concentration of iron cations present in this phase. It was expected that this method could lead to the maximum content of magnetite. Instead of that, it apparently failed to present any magnetite signs.

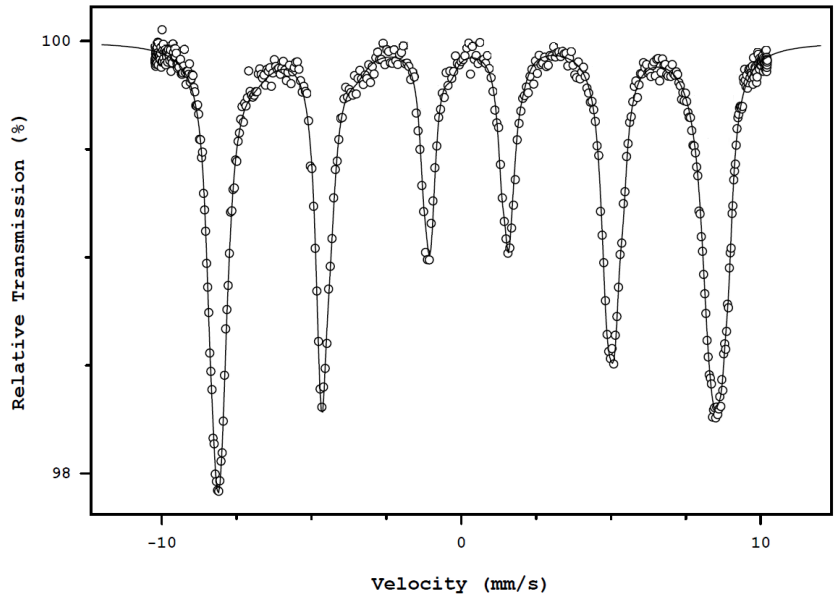


**Figure 28 – Mössbauer spectrum of a sample obtained by method AF, taken at 4.2 K.**

Surprisingly, it was method AF that led to the best overall results from this set of 3 methods. The obtained spectrum (figure 28) is typical of small sized maghemite particles, but the presence of an almost undetectable peak at -3.5 mm/s proves the presence of magnetite.

The average magnetic hyperfine fields of spectra taken at 4.2 K for samples prepared by methods AD (figure 26), AE (figure 27) and AF (figure 28) are about 49.9(3) T, 49.9(3) T and 49.5(3) T, respectively.

Overall, Mössbauer spectroscopy of the three methods revealed very identical spectra with somewhat unexpected results. None of the methods showed a clear improvement in the yield of magnetite over the standard method A from which they were derived. This proves that the mixing of iron ions with different valences is not the key factor for obtaining higher amount of magnetite.

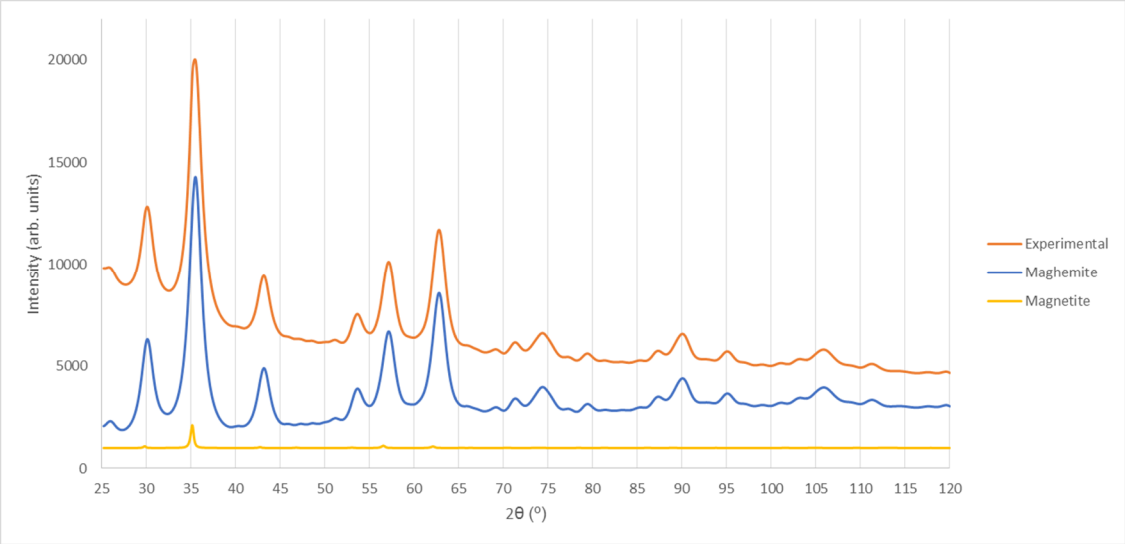


**Figure 29 – Diffractogram of a sample obtained by method AD.**

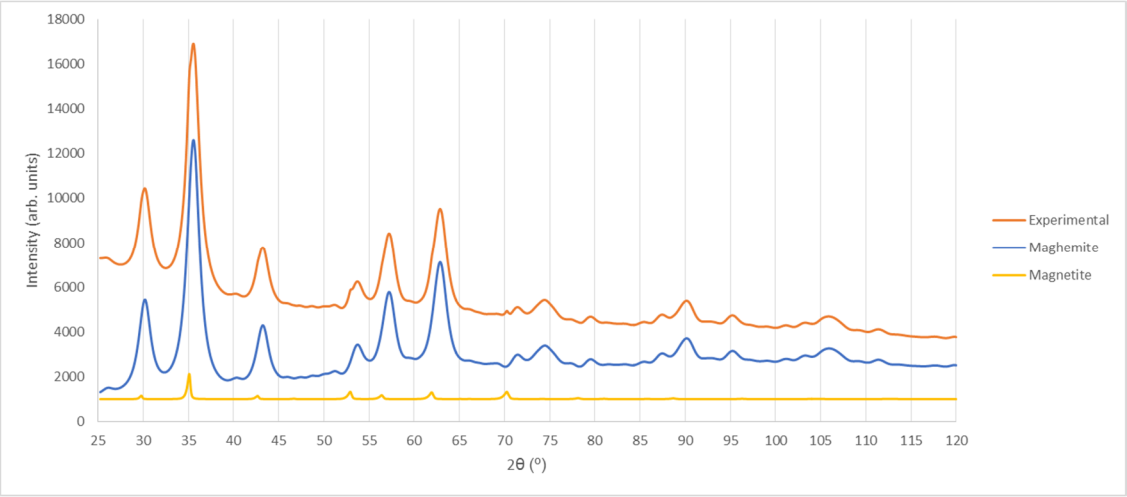


**Figure 30 – Diffractogram of a sample obtained by method AE.**

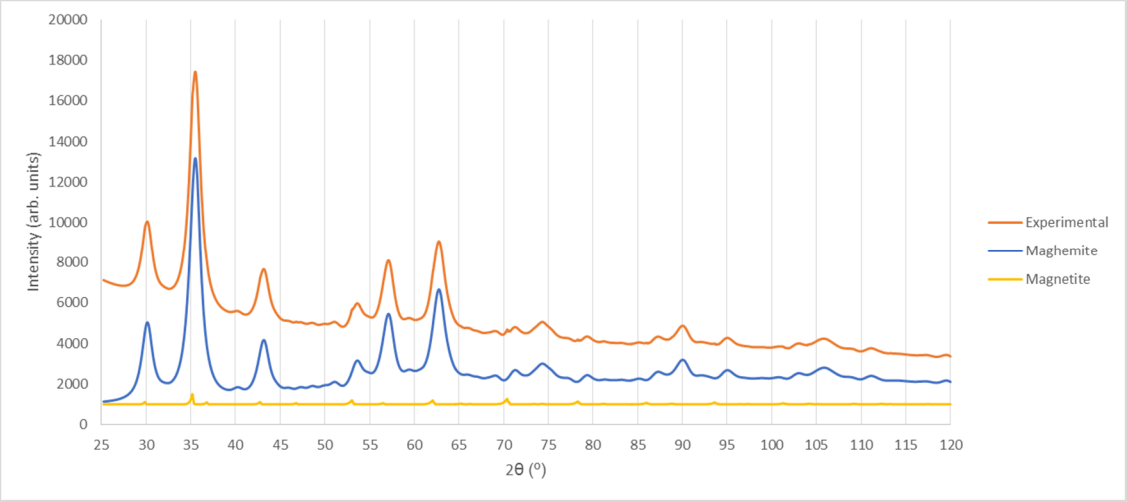


**Figure 31 – Diffractogram of a sample obtained by method AF.**

Diffractograms obtained for samples synthesized by methods AD (figure 29), AE (figure 30) and AF (figure 31) show maghemite as a major contributor. It's only when we calculate the lattice parameter associated with each sample that slightly significant differences begin to be noticed.

The results obtained from Mössbauer find a good correlation to those of XRD when we evaluate the lattice parameters of each sample. Between methods AD and AE, the difference is marginal. In the case of method AD, the material shows a lattice parameter value of *a*=0.8346(34) nm, and for method AE it has a value *a*=0.8335(25) nm, which are very close to the reference value of maghemite

(*a*=0.8347 nm). On the other hand, the product of method AF shows a lattice parameter value of *a*= 0.8351(55) nm, making it a mix of maghemite with magnetite as we expected to see from the previous Mössbauer analysis. Crystallite size remained almost identical between these three methods, with values of 5.5 nm for sample AD, 6.0 nm for sample AE and 6.9 nm for sample AF.

Overall, from all the three methods being discussed in this section, method AF proved to be the best. Although, no improvements were observed when compared with method A, having both very similar results.

## 4.4. Comparison of nanoparticles obtained from methods AG and D

Method AG was developed in order to understand how the nucleation time would affect particle size and their oxidation.

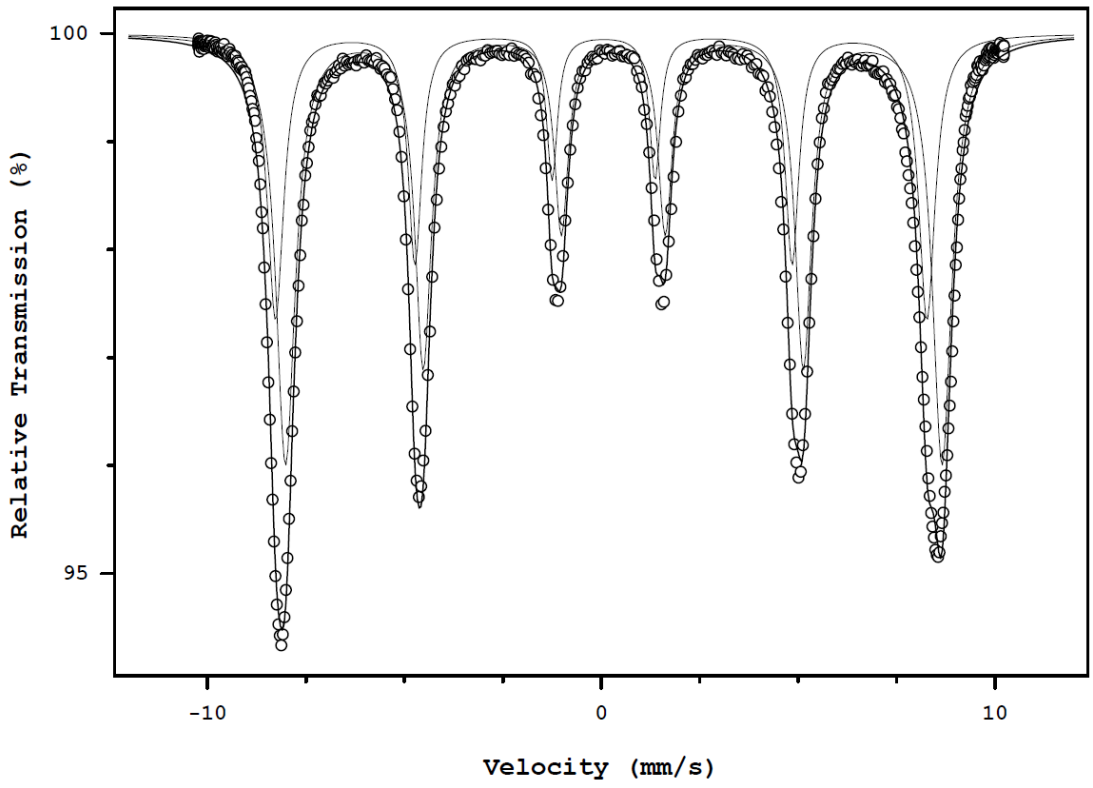


**Figure 32 – Mössbauer spectrum of a sample obtained by method AG, taken at 4.2 K.**

The Mössbauer spectrum of the sample obtained by method AG is correspondent to maghemite. It was fitted with two sextets whose hyperfine parameters are shown in table 6.

**Table 6 - Hyperfine parameters resulting from the fit to spectrum shown in figure 32.**

| Sites | IS (mm/s) | QS (mm/s) | H (T) | FHWM (mm/s) | % |
|---|---|---|---|---|---|
| **A (tetrahedral)** | 0.26(1) | -0.06(1) | 51.3(1) | 1.68(1) | 36.3 |
| **B (octahedral)** | 0.54(1) | 0.01(1) | 51.7(1) | 1.49(1) | 63.7 |

High values obtained for the magnetic hyperfine fields (H) indicate that a strong nanoparticle interaction exists [31].

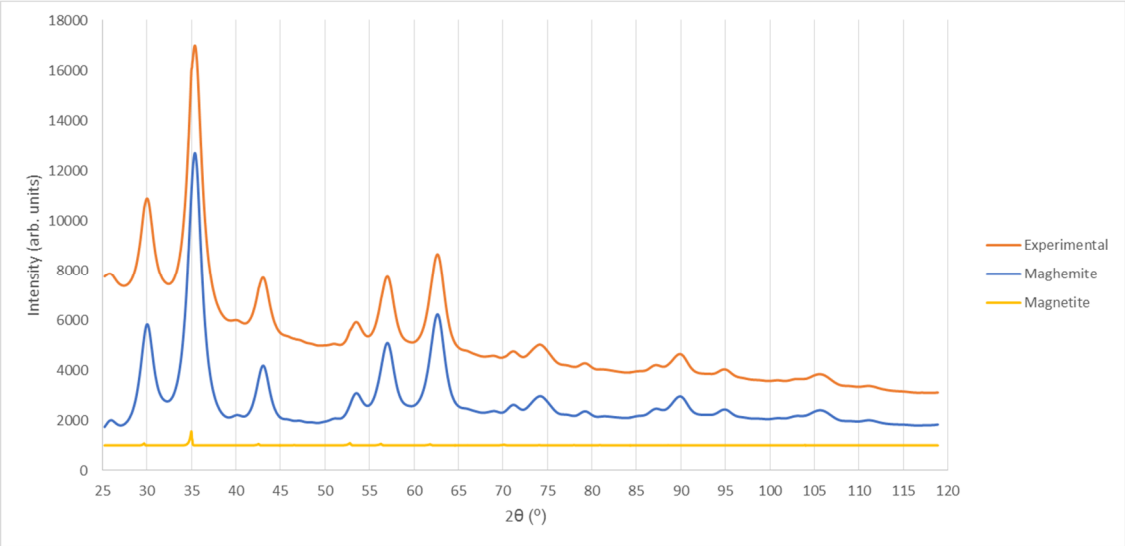


**Figure 33 - Diffractogram of a sample obtained by method AG.**

The diffractogram obtained for the sample synthesized by method AG (figure 33) shows maghemite as a major contributor, confirming the results obtained by Mössbauer spectroscopy. The lattice parameter value of *a*=0.8345(30) nm is almost the same as the reference value for maghemite (*a*=0.8347). This value was below those obtained for method A (*a*=0.8369(3) nm) and method AF (*a*=0.8351(55) nm). Crystallite size was identical to all the previous methods standing at 5.2 nm. Thus, increasing the time for nucleation does not have an effect in the size of the nanoparticles, so it can be inferred that the number of formed nuclei is similar.

Method D was developed to understand if the complete substitution of Oleylamine by Oleic Acid would change the product. The only difference between these two compounds is in the terminal groups.

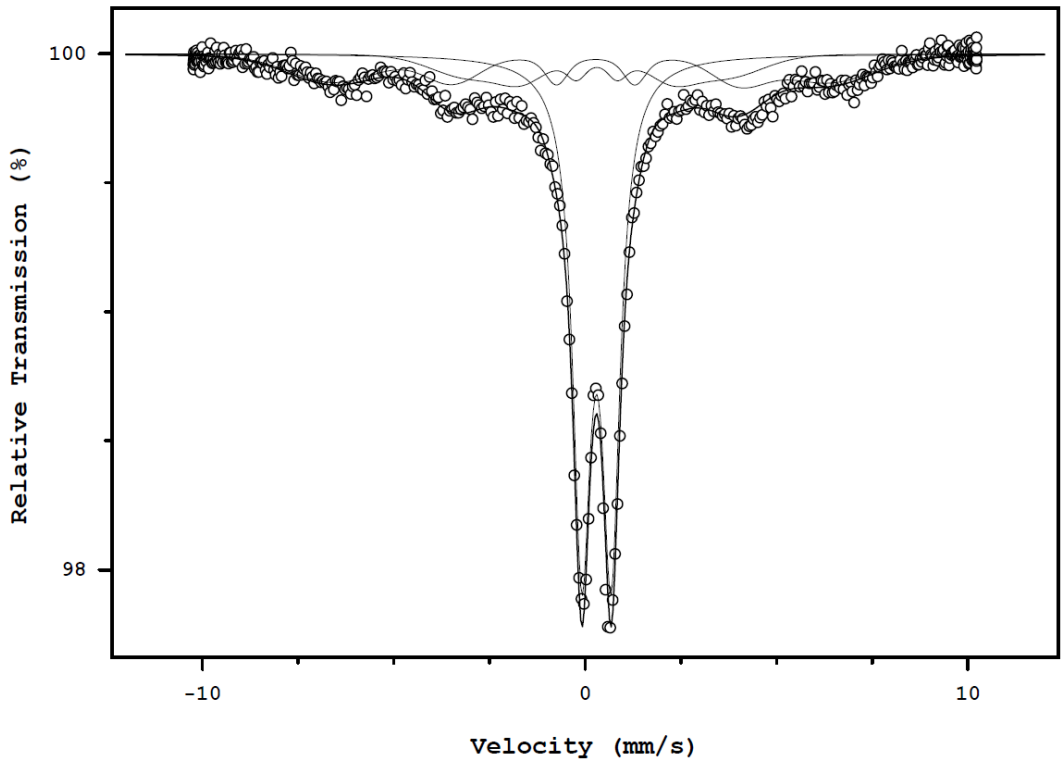


**Figure 34 - Mössbauer spectrum of a sample obtained by method D, taken at 4.2 K.**

The Mössbauer spectrum of the sample prepared by method D (figure 34) shows a doublet (59% of the spectrum) with hyperfine parameters of IS=0.53(1) mm/s and QS=0.77(2) mm/s, and two very broad sextets having magnetic hyperfine fields around 21 T and 40 T, respectively. This spectrum is completely different from those presented for magnetite or maghemite. It can be a result of the sample prepared by method D being composed by very small nanoparticles that are still superparamagnetic at 4.2 K.

## 4.5. Incorporation of the iron oxide nanoparticles in Amazonian essential oils

Essential oils of *Andiroba* and *Copaiba* were used to disperse the nanoparticles and prepare a biodegradable magnetic nanofluid. In this section,

we will discuss the effects that this medium has on the synthesized particles by method A and how it can affect the nanoparticles characteristics.

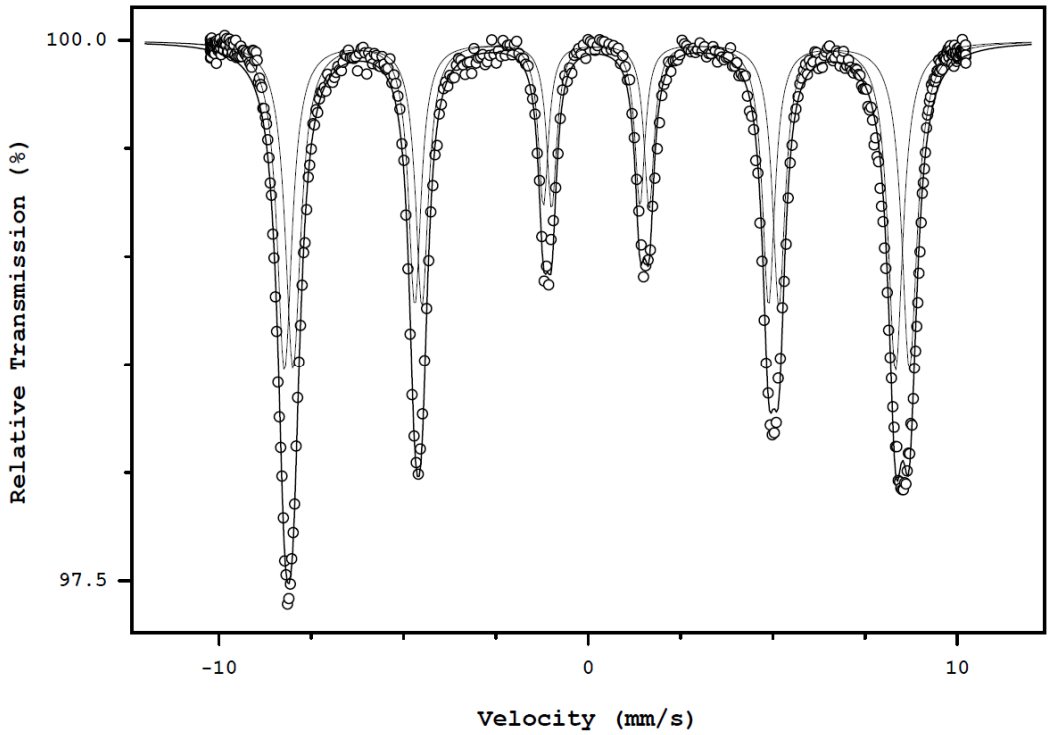


**Figure 35 - $^{57}$Fe Mössbauer spectrum, at 4.2 K, of a sample prepared by method A incorporating *Copaiba*'s oil.**

The Mössbauer spectrum of a sample obtained by method A incorporated in *Copaiba*'s oil (figure 35) didn't show any significant change when compared to the results of the sample obtained by method A standing alone (figure 18). Both show hyperfine interactions typical of maghemite. The magnetic hyperfine field (H) is higher than what was previous obtained for method A, indicating that a strong nanoparticle interaction exists [31].

The parameters obtained from the fitting procedure are shown in table 7.

**Table 7 - Hyperfine parameters resulting from the fit to spectrum shown in figure 35.**

| Sites | IS (mm/s) | QS (mm/s) | H (T) | FHWM (mm/s) | % |
|---|---|---|---|---|---|
| **A (tetrahedral)** | 0.30(1) | -0.05(1) | 51.3(1) | 1.64(1) | 49.4 |
| **B (octahedral)** | 0.57(1) | 0.02(1) | 51.8(1) | 1.69(1) | 50.6 |

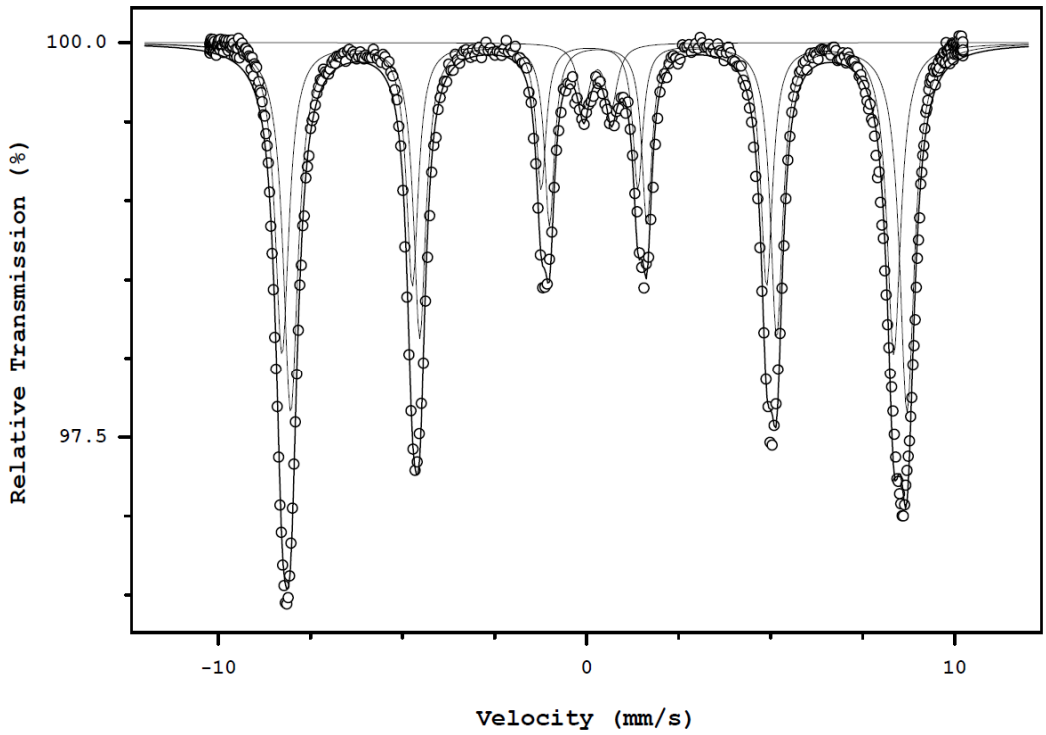


**Figure 36 - $^{57}$Fe Mössbauer spectrum, at 4.2 K, of a sample prepared by method A incorporating *Andiroba*'s oil.**

The Mössbauer spectrum of the sample obtained by method A incorporated in *Andiroba*'s oil (figure 36) deviates from what was expected. Contrary to what was obtained from the incorporation of *Copaiba*'s oil (figure 35), a doublet corresponding to $Fe^{3+}$ ions can be clearly seen in the central part of the spectrum.

The parameters obtained from the fitting procedure are shown in table 8.

**Table 8 - Hyperfine parameters resulting from the fit to spectrum shown in figure 36.**

| Sites | IS (mm/s) | QS (mm/s) | H (T) | FHWM (mm/s) | % |
|---|---|---|---|---|---|
| **A (tetrahedral)** | 0.29(1) | -0.04(1) | 51.5(1) | 1.52(1) | 41.9 |
| **B (octahedral)** | 0.56(1) | 0.01(1) | 51.9(1) | 1.61(1) | 54.1 |
| **$Fe^{3+}$ doublet** | 0.53(1) | 0.75(1) | - | 1.57(1) | 4.0 |

Also in table 8 the magnetic hyperfine fields (H) have high values compared to those obtained for method A, indicating a strong nanoparticle interaction [31].

Both *Andiroba*'s and *Copaiba*'s oils have been used in the preparation of some magnetic nanofluids [32]. The authors shown that in magnetic fluid-based oil *Andiroba*, the oleic acid molecules are tightly linked on the surface of

nanoparticles. The presence of carboxylic groups in the structure of diterpenic polymers in the oil, suggests the possibility of adsorption of these molecules on the surface of nanoparticles by means of complexation of carboxylate to $Fe^{3+}$ ions in the surface. However, the nanoparticles obtained by method A are surrounded by Oleylamine, so they are hydrophobic and not so available to interact with oil acids. Probably the oleic acid from the oil may join the Oleylamine coating and thus reach the nanoparticles. It is known that Oleic Acid interacts very well with Oleylamine, due to the long hydrophobic tail and the hydrophilic head in both compounds.

Both spectra (figure 35 and 36), in what concerns the Fe in tetrahedral and octahedral sites, seem to only be composed of maghemite, being the fit parameters in good agreement with this iron oxide.

Samples of nanoparticles of method A alone (sample A) and nanoparticles from method A incorporated in *Copaiba*'s oil (sample ACopaiba) and *Andiroba*'s oil (sample AAndiroba) were subjected to VSM analysis. We used this technique to observe how the synthesized nanoparticles would magnetically behave when incorporated in Amazonian essential oils.

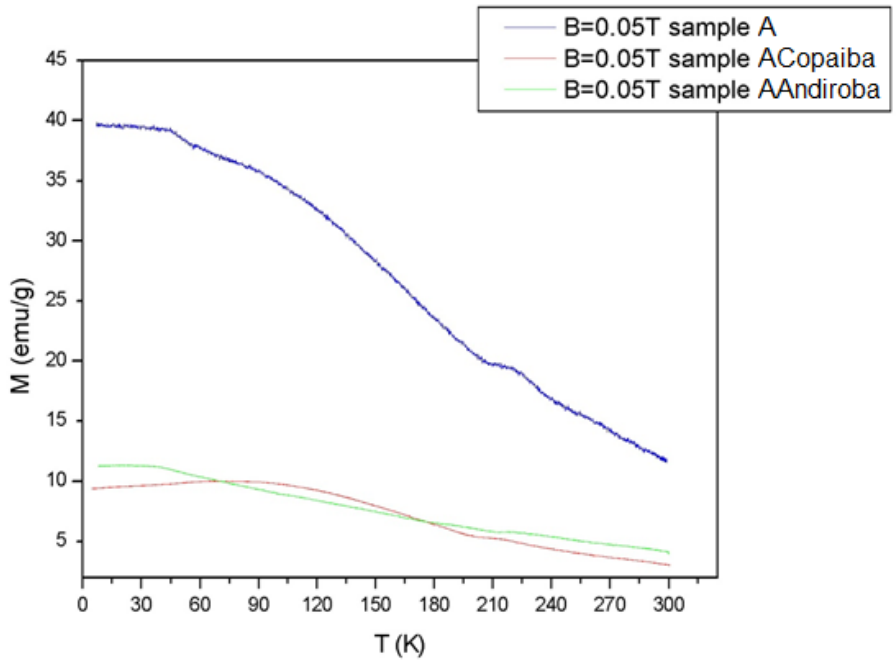


**Figure 37 - Field cooled curves of samples A, ACopaiba and AAndiroba.**

Field cooled (FC) magnetization curves of samples A, ACopaiba and AAndiroba were measured at 0.05 T as function of temperature, from 5 K to 300 K (figure 37).

FC curves for sample A are similar of those expected for a superparamagnetic behaviour. For samples ACopaiba and AAndiroba the temperature dependence shown for FC magnetization is not so strong.

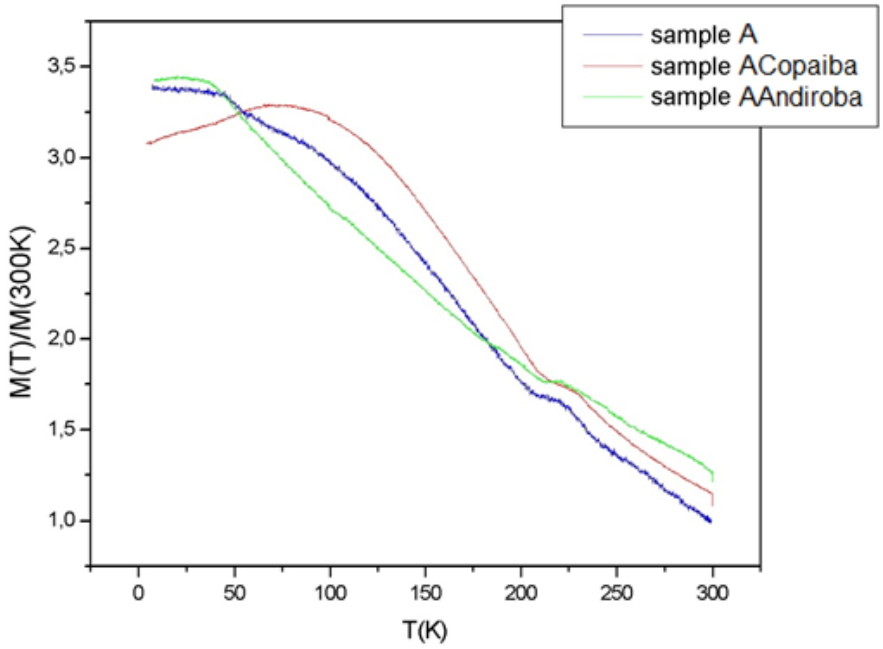


**Figure 38 - Representation of the ratio between magnetization and the value of magnetization obtained at 300 K as function of temperature, using data from figure 37.**

Even though all 3 samples have different FC curve shapes, all of them present a peak around 225 K (figure 38) which at this stage we are not able to explain.

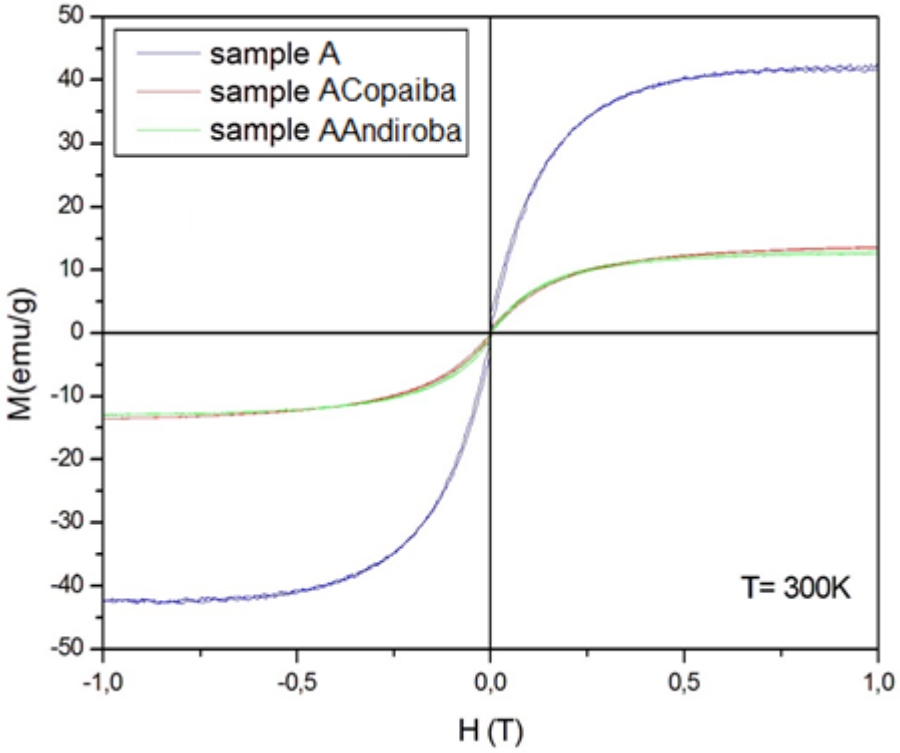


**Figure 39 - Magnetization measured as function of an applied field, at 300 K.**

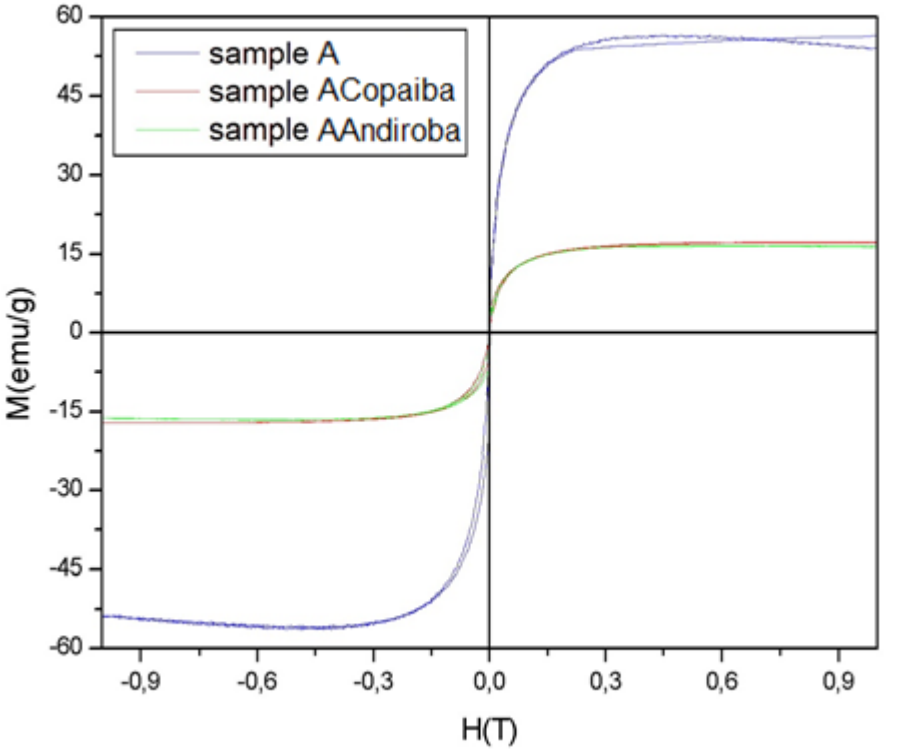


**Figure 40 - Magnetization measured as function of an applied field at low temperature (sample A and AAndiroba, at 7 K, and sample ACopaiba, at 5 K).**

Figures 39 and 40 show that magnetization saturation of samples ACopaiba and AAndiroba are much lower than that for sample A. Magnetization saturation obtained, at 300 K (figure 39), for our samples is about 42 emu/g, 14 emu/g and 12 emu/g, for samples A, ACopaiba and AAndiroba, respectively. At low temperature (figure 40), magnetization saturation of samples A, ACopaiba and AAndiroba is about 57 emu/g, 17 emu/g and 16 emu/g, respectively.

According to literature, magnetization saturation values found for maghemite particles with 5 nm is 35 emu/g at RT and 42 emu/g at 5 K [33]. The values obtained in this work for sample A are slightly higher than those obtained by Morales [33], but our value takes in account the particles interactions.

For bulk maghemite, in theory, a magnetization saturation of 77 emu/g at 5 K is expected. The reduction of magnetization saturation in nanoparticles is a surface phenomenon. At the surface of magnetic materials the spins are not as well ordered as are observed in the interior, and this leads to a surface layer with very small magnetization saturation. As the surface:volume ratios of nanoparticles are larger by a few orders of magnitude than those of conventional materials, the contribution of spin disorder at the surface to the magnetization is important and causes a significant reduction in magnetization saturation [27].

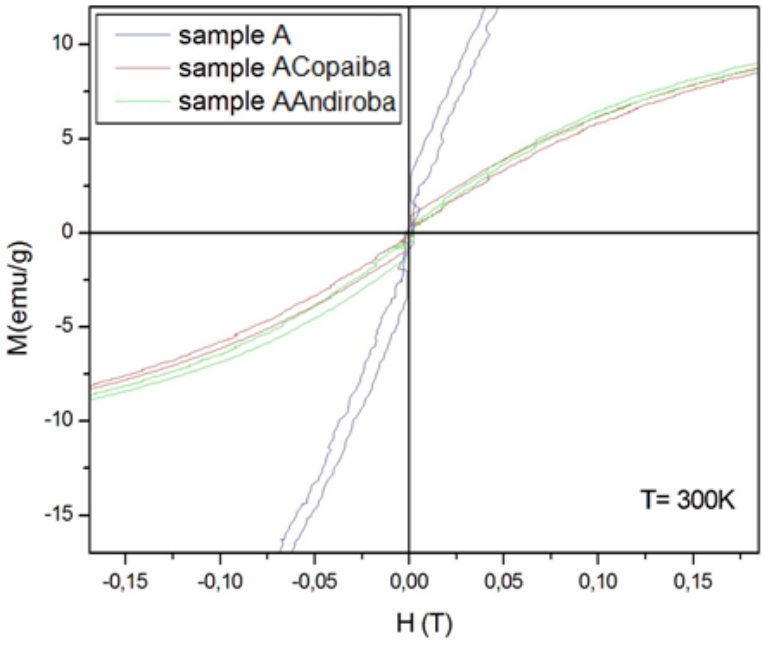


**Figure 41 - Details of hysteresis loops shown in figure 39.**

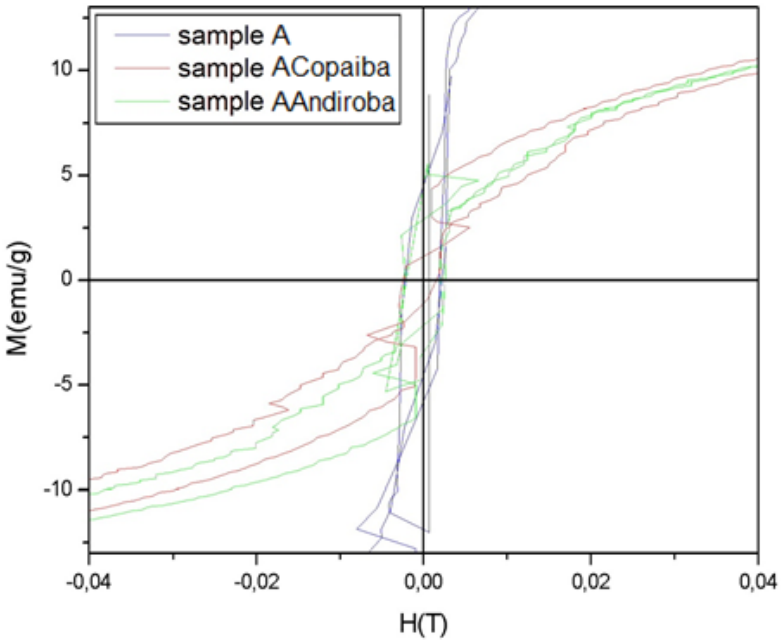


**Figure 42 - Details of hysteresis loops shown in figure 40 (sample A and AAndiroba, at 7 K, and sample ACopaiba, at 5 K).**

Figure 41 shows that the hysteresis curves are not reversible and that interparticle interaction exists. Of note, the coercive field is much larger for measurements at low temperature (figure 42).

With the magnetometer used, the determination of coercive field is very difficult as the variation of magnetization in fields near zero has fluctuations. As a results, it is not easy to control a slow variation of field for very low fields (about 100 Oe).

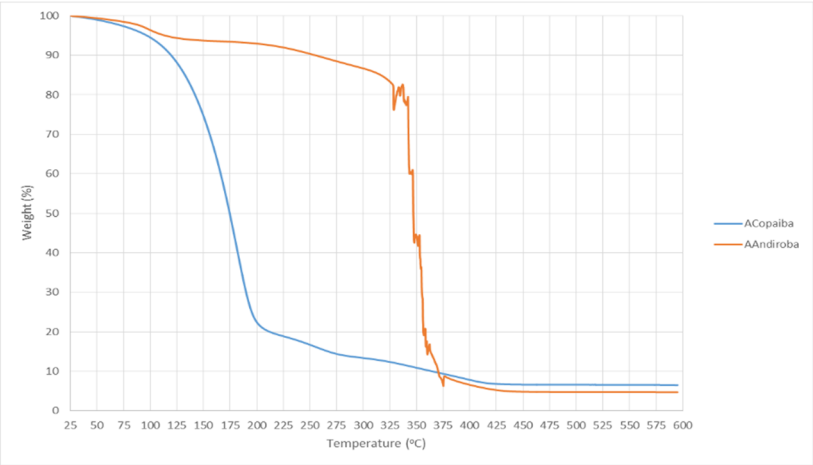


**Figure 43 - Thermograms of sample ACopaiba (blue) and sample AAndiroba (orange).**

Figure 43 presents the thermograms showing the difference between the thermal behaviour of each Amazonian oils with the nanoparticles. Of note, sample AAndiroba shows an erratic behaviour after 325ºC. Similar behaviour was found in highly energetic materials (exploding material) when some temperature highspots occurred, with melting and eruption of the material. In the oil, this can be due to the local combustion of some more energetic components. Despite this, AAndiroba has a higher degradation threshold than ACopaiba. The ratio between oil and particles is almost identical, with AAndiroba having 95:5 and ACopaiba having a ratio of 94:6.

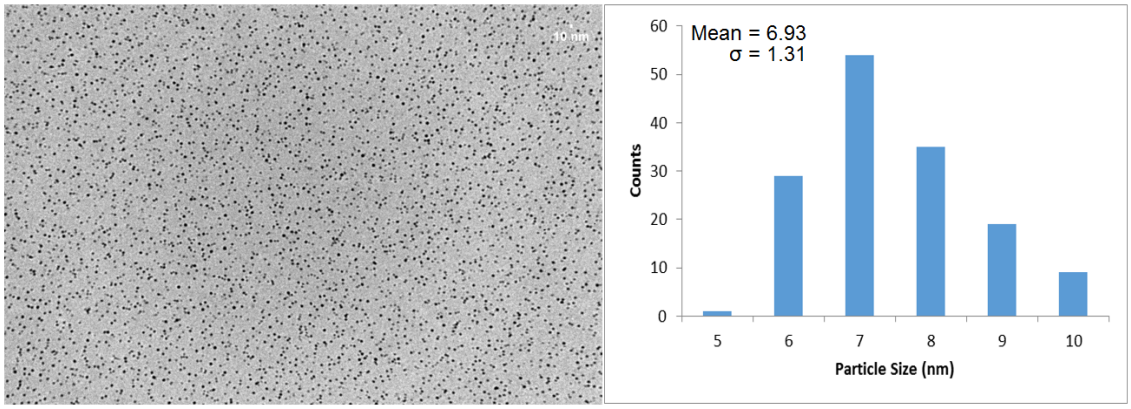


**Figure 44 - TEM image and respective size distribution calculation for sample ACopaiba.**

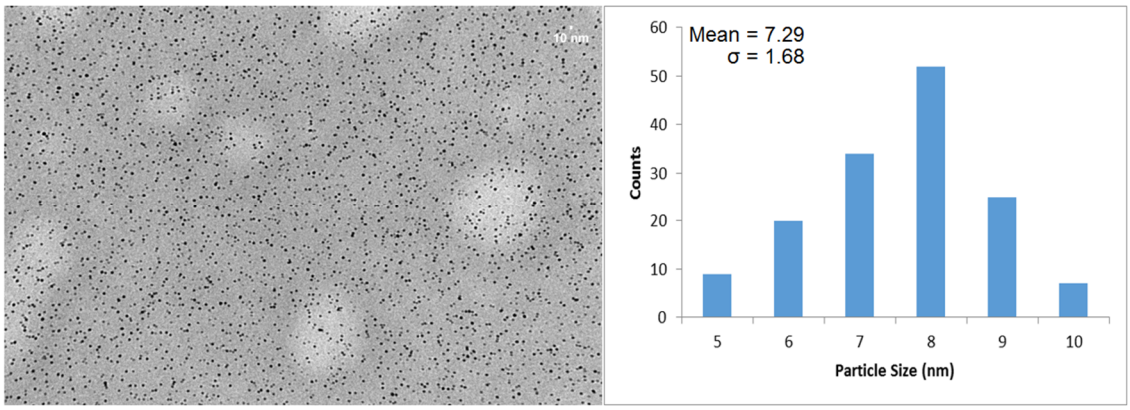


**Figure 45 - TEM image and respective size distribution calculation for sample AAndiroba.**

As can be observed in figures 44 and 45, samples ACopaiba and AAndiroba have very similar mean size distributions values: 6.93 nm and 7.29 nm, respectively. Comparing these results to those obtained for sample A (figure 24),

it can be concluded that the incorporation of the nanoparticles *Copaiba*'s or *Andiroba*'s oil doesn't affect their size, as expected.

A small test, where an external magnetic field (magnet) was applied to sample ACopaiba and AAndiroba, was performed to ascertain their magnetic behaviour.


**Figure 46 – Application of an external magnetic field to ACopaiba sample.**


**Figure 47 – Application of an external magnetic field to AAndiroba sample.**

Figure 46 and 47 show that both samples behave as a whole to the magnet. There isn't a separation between SPIONs and essential oil, both are attracted to the magnet. This shows a clear sign that we are before a nanofluid.

## 4.6. Evaluation of the iron oxide nanoparticles toxicity

As described in section 3.4.6, cytotoxicity tests were performed in nanoparticles synthesized according to method A.

**Table 9 – *In vitro* cytotoxicity and particle size, obtained from DLS, of PEG-PLA-nanoparticles in Caco-2 cells.**

| Formulations | $IC_{50}$ (µg/mL) | Particle size (nm) |
|---|---|---|
| PEG-PLA | > 500 | $137 \pm 5$ |
| PEG-PLA nanoparticles | > 500 | $153 \pm 1$ |

According to table 9, the lack of changes in $IC_{50}$ parameter between PGA-PLA polymer and PGA-PLA-nanoparticles is indicative of the very low cytotoxicity the iron oxide nanoparticles present. Also, obtained results from DLS show that PEG-PLA forms clusters with 2 iron oxide nanoparticles at most.

# 5. Conclusion and Future Work

In the present work, we studied several aspects on how to achieve the best possible biodegradable magnetic nanoprobe. In order to do this, 3 chemical synthesis methods (A, B and C) were first used to produce SPIONs, which were characterized by Mössbauer spectroscopy, XRD, TG and TEM.

These methods distinguished themselves by recurring to different literature. Method A followed the procedure described by Xu *et al*. [21] where Oleylamine acted as both reducing agent and stabilizer to produce SPIONs. Method C followed the procedure described by Sun *et al*. [22]. And method B followed our own interpretation of method C.

Initial XRD results showed that the nanoparticles from method A seemed more suitable for what we wanted to achieve. Despite having similar results, method B was far more expensive and no XRD results were obtained for the nanoparticles of method C. Mössbauer spectroscopy later revealed a fairly interesting spectrum for method C.

Next we devoted our time to study method A in more detail, by introducing some changes. Since magnetite has a 2:1 ratio of $Fe^{3+}$:$Fe^{2+}$ we tried to mimic this with the amount of initial iron precursor used in the reaction. Several $Fe^{3+}$:$Fe^{2+}$ ratios were tried and these gave rise to methods AD, AE and AF.

We concluded that the amount of iron precursors and their ratio had almost no effect on the iron phase obtained in the product. Surprisingly, according to the Mössbauer spectra obtained, method AF that had almost no $Fe^{3+}$ precursor achieved better results than methods AD and AE but not better than method A.

Next, we decided to investigate if the nucleation time would affect phase or particle size of the synthesis product. Method AG, which resulted from this idea, yield nothing new. Particle size and phase were maintained when compared to method A.

At this point, we pondered if Oleylamine could be completely substituted by Oleic Acid as the main synthesis surfactant, since both molecules show a very

identical chemical structure with exception to the terminal groups. Thus, method D was defined. Since we were unable to obtain results through XRD analysis, the future of this method seemed very dim. It was only when Mössbauer spectroscopy was performed that this method turned quite unique. The Mössbauer spectra suggests superparamagnetic nanoparticles with sizes below 5 nm.

One of the purposes of this work was to stabilize the SPIONs in Amazonian essential oils, which are biodegradable. Since method A maintained a superior quality of the product over all other methods, this method was chosen to produce the nanoparticles to be incorporated in *Copaiba*'s and *Andiroba*'s essential oils.

Results obtained for Mössbauer spectra were accordingly to what was expected, for the nanoparticles incorporated in *Copaiba*'s oil, as no change of phase was detected. The same can't be said to *Andiroba*'s oil with nanoparticles, since an unexpected $Fe^{3+}$ doublet was found in the Mössbauer spectrum. This can be possibly explained by interactions between the oil and the nanoparticles coating, forming $Fe^{3+}$ complexes.

VSM results showed similar magnetization saturation values for both oil samples with nanoparticles, but much smaller than for the nanoparticles alone. This indicates that there's a magnetic blocking effect by both Amazonian essential oils. This effect is possibly explained by the interaction originated between nanoparticles and the oil.

The non-reversibility found in the hysteresis curves in VSM as well as higher values of hyperfine magnetic field in Mössbauer, when compared with values obtained for SPIONs alone, indicate that when the particles are incorporated in Amazonian essential oils their superparamagnetic effect is reduced.

TGA thermograms revealed an oil to nanoparticles ratio of 95:5 to the sample incorporating *Andiroba*'s oil and a ratio of 94:6 to the sample incorporating *Copaiba*'s oil. Despite Mössbauer and VSM results revealing a strong particle interaction, TEM showed well dispersed nanoparticles in the oils, without any noticed increase in particle size in comparison to method A. A simple application

of an external magnetic field to samples incorporating Amazonian essential oils proved their behaviour as a nanofluid.

Finally, cytotoxic tests performed on the nanoparticles synthesized by method A revealed them to be most likely non-toxic for Caco-2 cells.

Concluding, it is of our understanding that a biodegradable magnetic nanoprobe can be assembled by using Amazonian oils and the iron oxide nanoparticles synthesized in this work. The narrow size distribution, biocompatibility of the particles and biodegradability of the Amazonian essential oils can constitute a novel route to perform magnetically assisted exams and cancer treatments.

Although, there are still some questions that were brought up during the course of this work and that can constitute future work to be done. One issue can be the further study of Oleic Acid as the only surfactant, since the obtained Mössbauer results were inconclusive.

Another possible work is to improve the study made by VSM of iron oxide nanoparticles incorporated, or not, in other oils or polymers. This would give us a better insight into what can be possibly causing the blocking effect that these particles suffer when incorporated in different mediums. Exploring the superparamagnetic effect, the associated coercive field and measuring the thickness of the coating would also be very interesting [34].

At last, a complete study of the cytotoxicity of iron oxide nanoparticles in Amazonian oils would strongly benefit the application of a biodegradable magnetic nanoprobe in the near future.

# 6. References


1. Lu, A.H., Salabas, E.L., & Schüth, F., *Magnetic nanoparticles: synthesis, protection, functionalization, and application.* Angewandte Chemie International Edition, 2007. 46(8): p. 1222-1244.
2. Lodhia, J., Mandarano, G., Ferris, N.J., Eu, P. & Cowell, S.F., *Development and use of iron oxide nanoparticles (Part 1): Synthesis of iron oxide nanoparticles for MRI.* Biomedical imaging and intervention journal, 2010. 6(2): p. e12.
3. Laurent, S., Dutz, S., Häfeli, U.O. & Mahmoudi, M., *Magnetic fluid hyperthermia: focus on superparamagnetic iron oxide nanoparticles.* Advances in Colloid and Interface Science, 2011. 166(1): p. 8-23.
4. Pacheco, T., Barata, L., and Duarte, M., *Antimicrobial activity of copaiba (Copaifera spp) balsams.* Ciência e Cultura, 1997. 49(5/6): p. 339-344.
5. Miranda Júnior, R.N.C., Dolabela, M.F., Silva, M.N., Póvoa,M.M. & Maia, J.G.S., *Antiplasmodial activity of the andiroba (Carapa guianensis Aubl., Meliaceae) oil and its limonoid-rich fraction.* Journal of ethnopharmacology, 2012. 142(3): p. 679-683.
6. Blundell, S., *Magnetism in Condensed Matter (Oxford Master Series in Physics)*. 2001: Oxford University Press, USA.
7. Jiles, D.C., *Introduction to Magnetism and Magnetic Materials, Second Edition*. 1998: Taylor & Francis.
8. Cornell, R.M. & Schwertmann, U., *The Iron Oxides: Structure, Properties, Reactions, Occurrences and Uses*. 2006: Wiley.
9. Schwertmann, U. & Cornell, R.M., *Iron Oxides in the Laboratory: Preparation and Characterization*. 2008: Wiley.
10. Koetz, J. & Kosmella, S., *Polyelectrolytes and nanoparticles*. 2007: Springer.
11. Belgacem, M.N. & Gandini, A., *Monomers, Polymers and Composites from Renewable Resources*. 2011: Elsevier Science.
12. Plowden, C., *Production ecology of copaíba (Copaifera spp.) oleoresin in the eastern Brazilian Amazon.* Economic Botany, 2003. 57(4): p. 491-501.
13. Sousa, J.P.B., Brancalion, A.P.S, Souza, A.B., Turatti, I.C.C., Ambrosio, S.R., Furtado, N.A.J.C., Lopes, N.P. & Bastos, J.K., *Validation of a gas chromatographic method to quantify sesquiterpenes in copaiba oils.* Journal of pharmaceutical and biomedical analysis, 2011. 54(4): p. 653-659.
14. Plowden, C., *The ecology and harvest of andiroba seeds for oil production in the Brazilian Amazon.* Conservation and Society, 2004. 2(2): p. 251.
15. Tappin, M.R.R., Nakamura, M.J., Siani, A.C. & Lucchetti, L., *Development of an HPLC method for the determination of tetranortriterpenoids in Carapa guianensis seed oil by experimental design.* Journal of pharmaceutical and biomedical analysis, 2008. 48(4): p. 1090-1095.
16. Vértes, A., Korecz, L., & Burger, K., *Mössbauer spectroscopy*. 1979: Elsevier Scientific Pub. Co.
17. Long, G.J. & Grandjean, F., *Mössbauer spectroscopy applied to magnetism and materials science*. 1993: Plenum Press.
18. Buschow, K.J. & De Boer, F.R., *Physics of magnetism and magnetic materials*. Vol. 92. 2003: Springer.

19. Cullity, B.D. & Graham, C.D., *Introduction to magnetic materials*. 2011: John Wiley & Sons.
20. Wang, Z.L., *Transmission Electron Microscopy of Shape-Controlled Nanocrystals and Their Assemblies.* The Journal of Physical Chemistry B, 2000. 104(6): p. 1153-1175.
21. Xu, Z., Shen, C., Hou, Y., Gao, H. & Sun, S., *Oleylamine as both reducing agent and stabilizer in a facile synthesis of magnetite nanoparticles.* Chemistry of Materials, 2009. 21(9): p. 1778-1780.
22. Sun, S., Zheng, H., Robinson, D.B., Raoux, S., Rice, P.M., Wang, S.X. & Li, G., *Monodisperse MFe2O4 (M= Fe, Co, Mn) nanoparticles.* Journal of the American Chemical Society, 2004. 126(1): p. 273-279.
23. Mosmann, T., *Rapid colorimetric assay for cellular growth and survival: application to proliferation and cytotoxicity assays.* Journal of immunological methods, 1983. 65(1): p. 55-63.
24. Roca, A.G., Marco, J.F., Morales, M.P., & Serna, C.J., *Effect of nature and particle size on properties of uniform magnetite and maghemite nanoparticles.* The Journal Of Physical Chemistry C, 2007. 111(50): p. 18577-18584.
25. McCammon, C., *Mössbauer spectroscopy of minerals.* Mineral physics & crystallography: A handbook of physical constants, 1995: p. 332-347.
26. Da Costa, G., De Grave, E., Bowen, L.H., De Bakker, P.M.A. & Vandenberghe, R.E., *Temperature dependence of the hyperfine parameters of maghemite and Al-substituted maghemites.* Physics and Chemistry of Minerals, 1995. 22(3): p. 178-185.
27. Gütlich, P., Link, R., & Trautwein, A., *Mössbauer spectroscopy and transition metal chemistry*. 1978: Springer-Verlag Berlin.
28. Murad, E. (1998). The characterization of soils, clays, and clay firing products. Hyperfine interactions, 111(1-4), 251-259.
29. Courtesy of Professor Friedrich Wagner, Technical University of Munich, Germany.
30. Berry, F.J., Skinner, S. & Thomas, M.F., *Mössbauer spectroscopic examination of a single crystal of.* Journal of Physics: Condensed Matter, 1998. 10(1): p. 215.
31. Vollath, D., *Nanomaterials: an introduction to synthesis, properties and applications*. 2013: John Wiley & Sons.
32. Silveira, L.B, Martins, Q.S., Maia, J.C. & Santos, J.G., *Preparation of Nanocomposites Resin from Seed Pterodon emarginatus Doped Maghemite Nanoparticles.* Journal of nanoscience and nanotechnology, 2012. 12(6): p. 4832-4835.
33. Morales, M.P., Andres-Verges, M., Veintmillas-Verdaguer, S., Montero, M.I. & Serna, C.J., *Structural effects on the magnetic properties of γ-$Fe_2O_3$ nanoparticles.* Journal of magnetism and magnetic materials, 1999. 203(1): p. 146-148.
34. Millan, A., Urtizberea, A., Silva, N. J. O., Palacio, F., Amaral, V. S., Snoeck, E., & Serin, V., *Surface effects in maghemite nanoparticles*, 2007. Journal of magnetism and magnetic materials, 312(1), L5-L9.